www.small-science-journal.com

Beyond Pristine Layers: Engineering van der Waals MPX₃ Materials (M: Transition Metal, X: Chalcogen) via Defects, Adsorption, and Intercalation

Yuriy Dedkov* and Elena Voloshina*

Recent breakthroughs and achievements in the studies of 2D materials have led to the increased attention to the respective van der Waals parent compounds. Herein, the class of layered materials—so-called transition metal phosphorus trichalcogenides (MPX₃; M: transition metal, X: chalcogen)—has been recently investigated extensively due to the diversity in their properties depending on the M/X combination. Moreover, further studies demonstrate the large tunability of the electronic, optical, and magnetic properties of these materials using different methods, like defects' engineering, alloying, adsorption, or intercalation. In the present review, several discussed approaches are focused on, highlighting the mechanisms leading to the properties' modifications and drawing perspectives on the further studies and developments in this class of materials.

1. Introduction

The increasing demand for low power consumption and miniaturization of functional elements in electronic and optical devices drives the search for new low-dimensional materials and systems—ideally 2D or 1D—that could serve as novel electrodes or insulating layers in such applications.^[1–3] Graphene, as a natural first choice among 2D materials due to its ease of isolation from bulk graphite or highly oriented pyrolytic graphite, ^[4] has been intensively studied since the discovery of its remarkable transport properties in 2005.^[5–7] Subsequent experimental and theoretical investigations have revealed numerous fascinating properties of graphene, including ambipolar electron and hole

Y. Dedkov Center for Advanced Laser Techniques Institute of Physics Bijenička cesta 46, 10000 Zagreb, Croatia E-mail: ydedkov@ifs.hr

E. Voloshina
Division of Theoretical Physics
Ruđer Bošković Institute
Bijenička cesta 54, 10000 Zagreb, Croatia
E-mail: elena.voloshina@irb.hr

The ORCID identification number(s) for the author(s) of this article can be found under https://doi.org/10.1002/smsc.202500307.

© 2025 The Author(s). Small Science published by Wiley-VCH GmbH. This is an open access article under the terms of the Creative Commons Attribution License, which permits use, distribution and reproduction in any medium, provided the original work is properly cited.

DOI: 10.1002/smsc.202500307

transport,[8] the quantum Hall effect at room temperature, substrate-protective capabilities, and long-distance spin transport, [12,13] among others. Studies on bilayer and multilayer graphene have further shown that these systems provide a versatile platform for exploring exotic physical phenomena such as bandgap tuning [14] and twist-angle-dependent superconductivity. [15,16] Despite these intriguing features, several limitations—such as graphene's zero bandgap, lack of intrinsic magnetic ordering, and challenges in achieving high material quality-hinder the practical application of single-, bi-, and multilayer graphene in advanced technologies. These limitations underscore the need

for new mono- and multiatomic layered materials. This pursuit has recently led to the isolation and in-depth exploration of the electronic, optical, and magnetic properties of alternative 2D materials, including silicene, phosphorene, and transition metal mono-, di-, and trichalcogenides.^[17–20]

Among the various 2D and layered materials, transition metal phosphorus trichalcogenides (TMTs)—represented by the structural formula MPX₃ (where M is a transition metal, P is phosphorus, and X is a chalcogen)—have attracted growing interest. Their properties have been comprehensively reviewed in several recent publications.^[20–23] Owing to the diversity of their electronic and magnetic structures across different MPX₃ compounds, a wide range of potential applications has been proposed. These include low-dimensional ferroelectricity,^[24,25] their use in Li- and Mg-ion batteries,^[26,27] water splitting technologies,^[28,29] and hydrogen storage.^[30,31]

In general, MPX₃ compounds are wide-bandgap semiconductors in which bandgaps depend on the specific combination of M and X atoms.^[20,32] This family includes materials that exhibit various magnetic configurations of M²⁺ ions in their antiferromagnetic (AFM) ground states. The magnetic interactions between neighboring M²⁺ ions arise from a competition between direct AFM exchange and indirect ferromagnetic (FM) exchange mediated via the chalcogen atoms. In most studied MPX₃ systems, the AFM interaction dominates, determining the ground magnetic state. However, both theoretical predictions and experimental confirmations have shown that the magnetic ground state can be tuned—either by suppressing the direct AFM exchange (e.g., through alloying) or by enhancing the indirect FM exchange (e.g., via electron or hole doping). Furthermore, the electronic structure of these materials can be engineered to

www.small-science-iournal.com

www.advancedsciencenews.com

adjust the bandgap and induce novel states, such as massless Dirac fermions in doped compounds.

Given the broad range of potential applications and tunable properties of MPX3 materials, this review focuses on specific examples illustrating how their electronic and magnetic structures can be modified in a controlled manner (Figure 1). We highlight several key approaches—such as defect engineering, adsorption, alloying, and intercalation—that have been successfully employed to tailor their properties. Both theoretical and experimental advances are discussed, with an emphasis on representative case studies. Finally, we outline future directions that may enable the discovery of new phenomena and further expand the application space of MPX₃ materials.

2. Ground State Properties of Bulk MPX3

The synthesis methods and various properties of MPX₃ materials have been comprehensively reviewed in several recent publications. [20-23] Here, we briefly summarize only the aspects most relevant to the subsequent discussions.

MPX₃ layered crystals are usually arranged in the C2/m and $R\overline{3}$ space groups for X = S and Se, respectively. Every single layer is built from M²⁺ ions arranged in a honeycomb lattice, and every hexagon is centered by a P-P dimer perpendicular to the layer, forming [PX₃]²⁻ pyramids above and below the layer (Figure 2A). Thus, every layer is terminated by chalcogen atoms, leading to weak van der Waals (vdW) interactions between layers. Following the crystallographic structure of MPX₃, one can see that three types of chemical bonds-ionic, covalent, and vdW

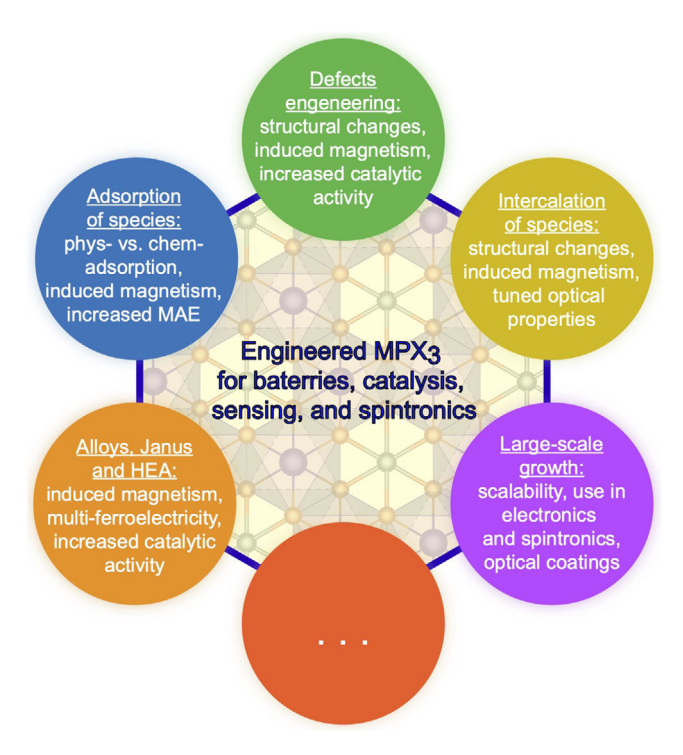


Figure 1. Strategies currently used to modify the properties of vdW MPX₃ materials for their applications in various fields, highlighting several modified or induced properties.

—are responsible for the formation of the electronic structure of these materials, challenging the correct description of their electronic properties.^[20] The representative high-resolution transmission electron microscopy (TEM) images of several MPX₃ materials are shown in Figure 3. [33-36]

All MPX₃ materials are wide-bandgap semiconductors. Among them, the MPX₃ compounds consisting of open *d*-shell M²⁺ ions are antiferromagnetically ordered, demonstrating different types of magnetic ordering; e.g., MnPS3 is a Heisenberg-type Néel AFM with $T_N = 87$ K, while FePS₃ exhibits Ising-type zigzag AFM ordering with $T_N = 118$ K, etc. [37–39] (Figure 2B). Along with that, TMTs that include two transition metal ions, such as CuCrP₂S₆, where the ionic charge states are Cr³⁺ and Cu¹⁺, exhibit intralayer FM ordering of Cr magnetic moments and AFM coupling between neighboring layers. [40,41] The magnetic ordering of M²⁺ or M³⁺ ions in a single-MPX₃ layer is the result of the competition between exchange couplings among the first, second, and third nearest-neighbor (NN, 2NN, and 3NN) localized spins, respectively. In turn, the NN exchange interaction I_1 arises from the competition between direct M-M exchange and M-X-M superexchange interactions (Figure 2B). The direct M-M exchange is always AFM, determined by the overlap of *d* orbitals, whereas the M-X-M superexchange interaction is always FM due to the M-X-M bond angle being close to 90°, following the well-known Goodenough–Kanamori–Anderson rules [42–44] (Figure 2B). Therefore, as a first perspective from this consideration, one can expect that the magnetic state of originally AFM-ordered MPX₃ compounds can be tuned and converted to a FM state if the M-X-M superexchange interaction begins to dominate over the direct M-M coupling. This can be realized in different ways, as will be discussed further.

The electronic structure of different MPX3 compounds has been rigorously studied in a series of recent experimental and theoretical works. Although several inconsistent and nonsystematic studies can be found in the literature (see discussion in ref. [20]), the current consensus is that most of these compounds are wide-bandgap semiconductors and, in the case of magnetic M²⁺ ions, exhibit AFM ordering. The calculated and measured bandgaps for these materials vary between 1.2 and 3.5 eV, depending on the specific M and X elements (see examples of the calculated band structures in Figure 2C). Using various experimental techniques in combination with theoretical analysis, these materials have been classified into several types of insulating states according to the Zaanen-Sawatzky-Allen scheme^[45]: MnPX₃, FePX₃, and CuCP₂S₆ are described as Mott–Hubbard insulators ($\Delta > U_{dd}$)^[37,41,46–53]; NiPS₃ is classified as a charge-transfer insulator ($\Delta < U_{dd}$)^[46,50,54]; and CoPS $_3$ shows intermediate behavior ($\Delta \approx U_{dd}$). [55,56] Here, Δ denotes the charge-transfer energy between the metal d-states and ligand (chalcogen) p-states, while U_{dd} represents the on-site Coulomb repulsion energy for the 3*d* states. Recent spectroscopic studies of these compounds have provided a more complete understanding of their electronic structure and have enabled detailed tracking of changes in the electronic properties across AFM phase transitions.

The most common method for synthesizing high-quality MPX₃ materials is chemical vapor transport (CVT). [20,21,57] In this approach, the appropriate amounts of elements, in the correct molar ratio (M:P:X = 1:1:3), are mixed and sealed in an evacuated

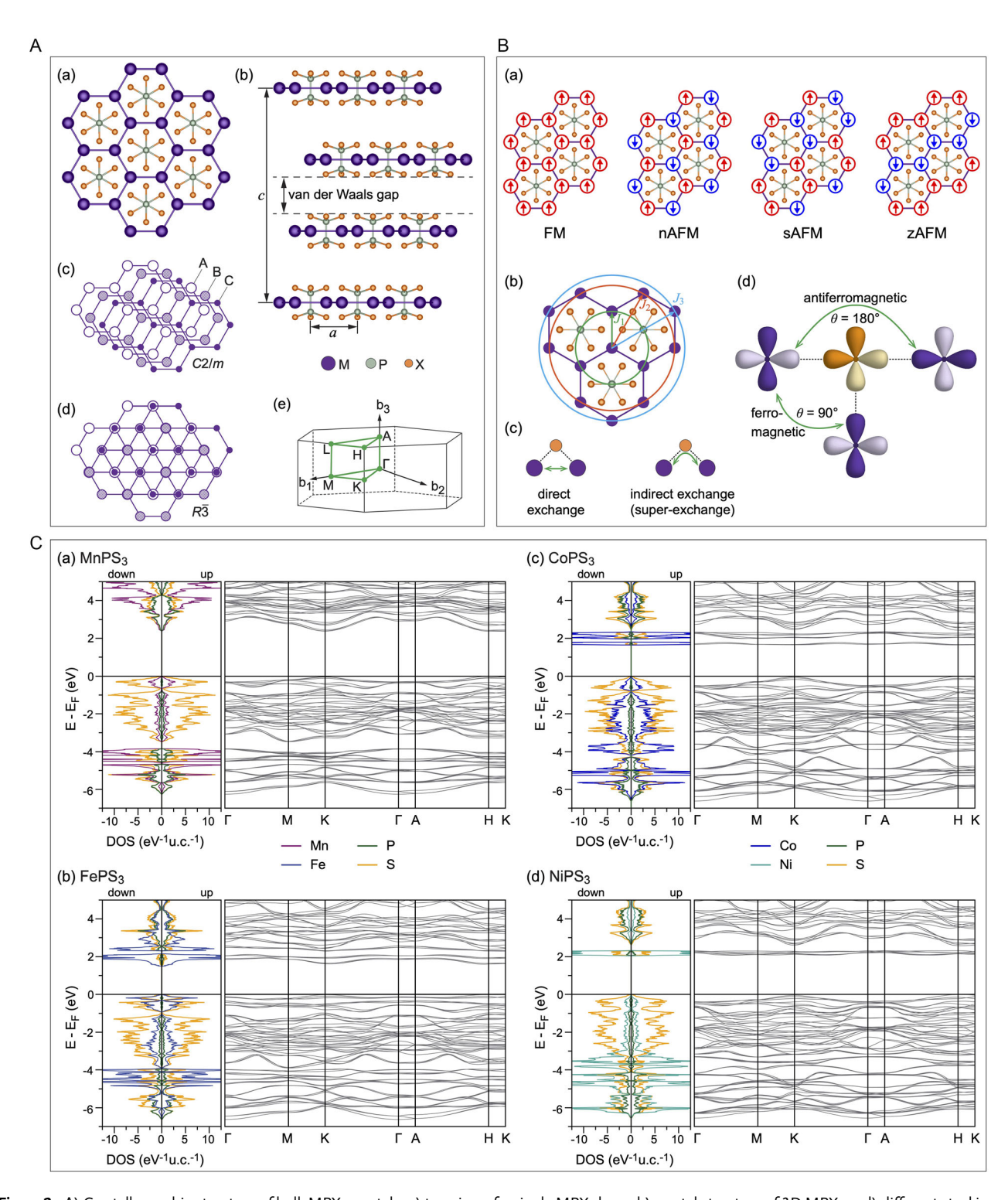


Figure 2. A) Crystallographic structure of bulk MPX₃ crystals: a) top view of a single MPX₃ layer; b) crystal structure of 3D MPX₃; c,d) different stackings in bulk MPX₃ corresponding to C2/m and $R\overline{3}$ space groups, respectively. For simplicity, only M-ions are shown. Atoms of different layers are shown with spheres of different size and style; e) Brillouin zone for 3D MPX₃ in the hexagonal representation. B) Magnetic structures of single MPX₃ layers: a) four different magnetic configurations of 2D MPX₃: ferromagnetic (FM), Néel antiferromagnetic (nAFM), stripy antiferromagnetic (sAFM), and zigzag antiferromagnetic (zAFM); b) the Heisenberg coupling parameters J_1, J_2 , and J_3 in the MPX₃ lattice; c) schematic representation of direct (M–M) and indirect superexchange (M–X–M) interactions, respectively; d) schematic representation of the FM and AFM coupling between M-ions via ligand according to the Goodenough–Kanamori rules. C) Calculated atom projected DOS and band structures for bulk MPX₃ crystals: a) MnPS₃; b) FePS₃; c) CoPS₃; d) NiPS₃. Reproduced with permission. (20) Copyright 2023, IOP Publishing.

s-and-conditions) on Wiley Online Library for rules of use; OA articles are governed by the applicable Creative Commons License

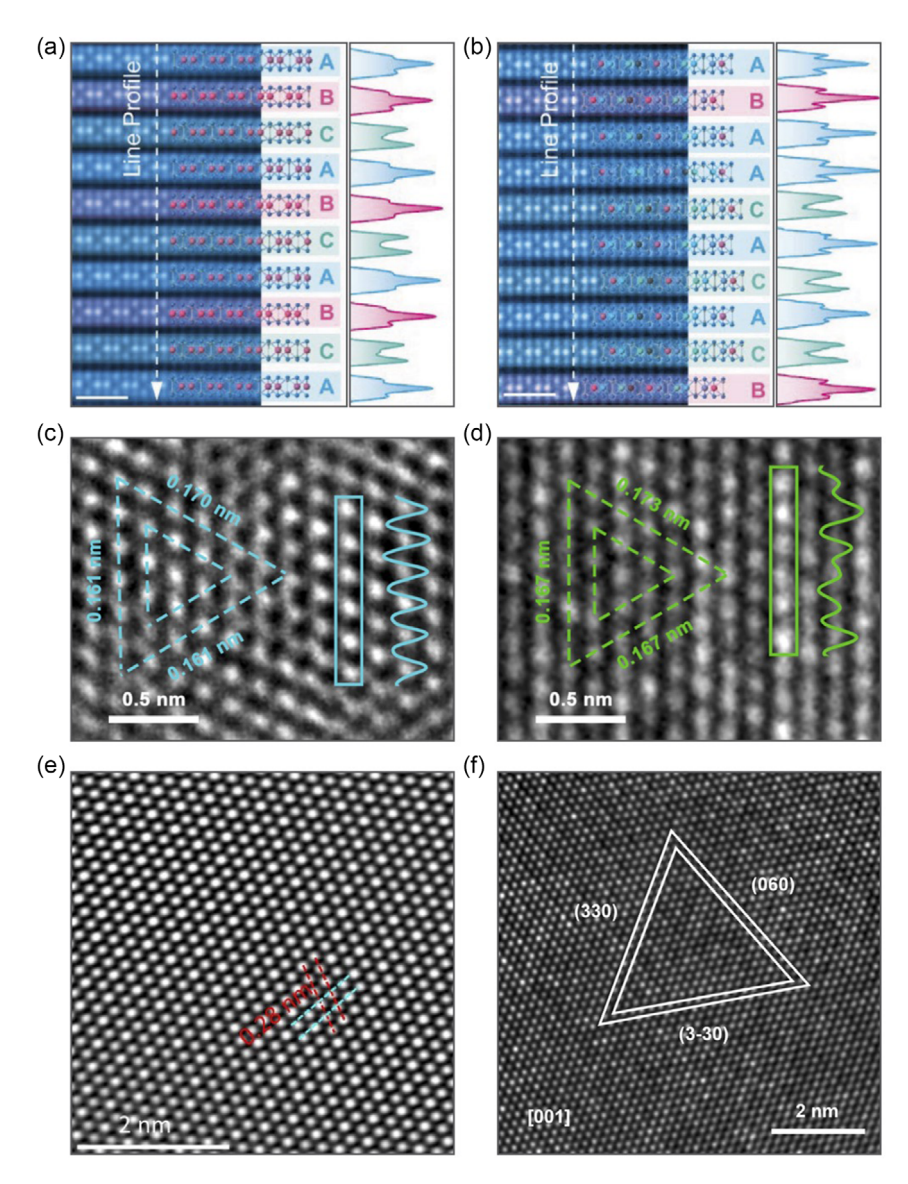


Figure 3. a,b) Cross-sectional scanning TEM annular dark-field images showing an ordered ABC stacking sequence in FePS₃ (left panel) and an aperiodic stacking order in FeMnNiVZnPS₃ (right panel). Corresponding intensity line profiles are also presented. Reproduced with permission. ^[33] Copyright 2024, John Wiley and Sons. c,d) High-resolution scanning TEM images and the respective intensity profiles for CoPS₃ (left panel) and Co_{0.6} (VMnNiZn)_{0.4}PS₃ (right panel). Corresponding intensity line profiles are also presented. Reproduced with permission. ^[34] Copyright 2022, American Chemical Society. e,f) High-resolution TEM images of NiPS₃ (left panel) and NiFePS₃ (right panel). Reproduced under the terms of the Creative Commons Attribution 4.0 license. ^[35] Copyright 2023, The Authors. Published by IOP Publishing. Reproduced with permission. ^[36] Copyright 2022, John Wiley and Sons.

quartz ampule, with a small amount of I_2 typically added as a transport agent. The sealed ampule is then placed in a two-zone furnace, where a specific temperature gradient and time are applied to produce high-quality samples up to $1\,\mathrm{cm}^2$ in size (see refs. [20,21,32]). However, the wide-bandgap nature of these materials leads to some experimental challenges, e.g., in electron spectroscopy experiments, primarily due to potential charging effects in bulk or thick MPX₃ samples (even during proper handling and mounting) or sample inhomogeneities that may occur during cleavage. These challenges can be addressed through various strategies, such as transferring very thin layers onto conductive supports; however, this introduces uncontrollable interfaces

between the MPX₃ layers and the substrate. A recently developed modified chemical vapor deposition technique for growing MPX₃ layers on SiO_2/Si substrates, as well as on fluorine-doped tin oxide and indium tin oxide glass substrates, has shown promise in overcoming these issues. [58,59] Nevertheless, further experimental development is required for the large-scale production of thin MPX₃ layers, potentially up to several square millimeters.

3. Modifications of MPX₃ Materials

This section provides an overview of the three main approaches currently proposed and employed for the functionalization of



www.small-science-iournal.com

various vdW MPX3 materials, aiming to enhance their performance in different application areas. These approaches, along with corresponding references and brief results of the respective MPX₃ modifications, are summarized in **Table 1**, with emphasis on recent experimental and theoretical works.

3.1. Defects Formation and Stability

The creation of vacancies in MPX₃ materials is a natural method for tailoring their electronic, magnetic, and optical properties. At the same time, it is expected that chalcogen or phosphorus vacancies may easily form during the exfoliation of MPX3 samples, potentially altering their properties and affecting the interpretation of observed phenomena. In a series of works, [37,60,61] systematic density functional theory (DFT) calculations were performed for various chalcogen vacancy configurations in layers of MnPX₃ (Figure 4), NiPX₃, and CrPX₃. It was found that the formation energy for S and Se vacancies lies in the range of \approx 1.2 – 1.6 eV, indicating a high likelihood of their formation during exfoliation. Furthermore, for the same defect type, Se vacancies are more likely to form than S vacancies, which correlates with their respective electronegativity values.

In the case of MnPX₃ (Figure 4), it was found that if chalcogen vacancies appear within the same X-layer, the resulting redistribution of electron density leads to a very weak ferrimagnetic state in MnPX₃, with net total magnetic moments of $\approx 0.001 \mu_B$ (X: S) and $0.002\mu_B$ (X: Se). [37] However, the formation of X-vacancies in different chalcogen layers does not affect the AFM state of the MPX₃ materials. The presence of such defects results in the emergence of midgap states in the case of double chalcogen vacancies within the same layer and leads to a reduction of the bandgap of MnPX3 in all studied cases. Surprisingly, no significant redistribution of electronic states in the valence or conduction bands of MnPX3 was observed, which leads to almost identical light absorption spectra for both pristine and defected MnPX₃. Therefore, it was concluded that optical spectroscopy is not the most effective method for assessing the quality of MnPX₃ materials and studied samples, and that further experimental techniques must be developed for this purpose.

The formation of X- and P-vacancies in MnPX₃, FePS₃, and NiPS₃ upon irradiation with a high-energy electron beam in TEM experiments was observed in refs. [62-64]. Corresponding simulations of the electron beam interactions with these materials showed that X-vacancies form at significantly lower acceleration voltages compared to P-vacancies—≈60 keV versus 95 keV, respectively—an effect that is clearly related to the crystallographic structure of MPX₃ layers. Notably, both of these energy thresholds are considerably lower than those required to create vacancy defects in graphene, which is a critical factor in the context of TEM investigations. It should also be noted that prolonged electron beam irradiation leads to the gradual degradation and decomposition of MPX3 layers. Extended exposure results in a change in the sulfur concentration within the layer, followed by oxidation driven by residual gases present in the microscope environment.[62]

It is interesting to consider the observation of the so-called "parasitic" ferromagnetism in few-layered MnPS3 prepared via liquid exfoliation, [65] which was also attributed to the formation of vacancies in this material. The MnPS₃ samples were produced by stirring CVT-grown crystals in a KCl solution, followed by centrifugation and decantation. The resulting few-layered MnPS₂ exhibited very weak FM ordering below a transition temperature of 38 K, which was explained by the formation of Mn-vacancies introduced during the exfoliation process. However, considering the crystallographic structure of MnPS₃, the formation of vacancies within the central Mn layer of the lattice without causing structural disintegration of the entire crystal appears unlikely. Instead, the formation of S- and P-vacancies during synthesis is more plausible. Nevertheless, as was demonstrated theoretically^[37] and discussed earlier, such vacancies in MnPS₃ are not expected to generate a significant magnetic moment. The most probable mechanism for the emergence of weak ferromagnetism in MnPS₃ is the intercalation of Li ions between the layers during the sample preparation process described above, which can lead to the ion-exchange process with formation of Mn vacancies in the MnPS₃ layers. This interpretation is supported by the observed increase in interlayer spacing-from 6.51 Å in bulk $MnPS_3$ to 7.55 Å in the few-layered samples. [65] As will be discussed in more detail in Section 3.2 and 3.3, Li intercalation can also lead to the effective doping the MnPS3 layers, leading to an enhancement of the Mn-S-Mn FM superexchange interaction for the I_1 NN coupling. This enhancement can overcome the intrinsic AFM direct exchange, resulting in the observed weak ferromagnetism. Further details of possible mechanism are presented below.

The interesting situation was found for defects formation in layers of NiPX3. $[{}^{\check{60}}]$ In this systematic DFT calculations, the formation of the double-X vacancies in NiPX3 is found to be more energetically favorable compared to other types. In this case, the removal of a chalcogen atom breaks the bond, and the remaining electron occupies the easily available electronic states of a (P₂X₅) entity. As a result, a localized defect state appears in the energy gap just at the top of the valence band, and the electron density is delocalized between the P and X atoms of the defective sublayer. Also, one more state is formed in the energy gap between the valence and conduction bands, and it has Ni 3d character. The magnetic moments of the Ni²⁺ ions near the vacancy are coupled ferromagnetically, and both considered states appear in the spinup channel. Naturally, these changes in the electronic structures of both materials lead to the decrease of the energy gap width to 1.36 eV/1.29 eV for the defective NiPS₃/NiPSe₃, compared to 2.19 eV/1.85 eV for pristine NiPS₃/NiPSe₃, respectively. These theoretical findings were confirmed by the experimental observations of FM order in Ni_{1-x}Co_xPS₃ caused by the formation of Svacancies^[66] (Figure 5). Here, $Ni_{1-x}Co_xPS_3$ nanosheets (NS) were synthesized via the chemical vapor conversion method, and it was demonstrated that a weak FM ground state in these compounds is formed at low temperatures, with a transition temperature depending on x: it gradually increases from 25 to 110 K, when x is changed from 0 to 0.4. The respective theoretical analysis shows that the presence of S-vacancies in Ni_{1-x}Co_xPS₃ is responsible for the suppression of long-range AFM order, while other competing FM interactions start to dominate at low temperatures. The corresponding DFT calculations show that the charge redistribution around S-vacancies leads to an uncompensated magnetic moment of $\approx 0.17 \mu_B/f.u.$ In this case, the imbalance between spin-up and spin-down electrons in two

www.small-science-journal.com

Table 1. An overview of approaches to modifying the various MPX₃ materials discussed in this review.

Modification	MPX_3 material	Study approach	Result of modification	References
Defects				
X-vacancy	$MnPX_3$	Theory	Reduction of the bandgap; emergence of midgap states	[37,76]
	NiPX ₃	Theory	Reduction of the bandgap; emergence of midgap states; formation of FM state	[60]
	$Ni_{1-x}Co_xPS_3$	Experiment	Formation of FM state as a result of formation of S-vacancies during samples' synthesis	[66]
	$CrPX_3$	Theory	Insignificant effect on electronic/magnetic properties	[61]
X/P-vacancy	MnPX ₃ FePS ₃ NiPS ₃	Experiment	Prolonged electron beam irradiation leads to the gradual degradation and decomposition of MPX ₃ layers	[62-64]
	$MnPS_3$	Experiment	Transformation into cubic α -MnS alloyed with P	[63]
	$MnPSe_3$	Experiment	Formation of mixed α -MnSe and γ -MnSe phases	[63]
	FePS ₃	Experiment/ theory	Reduction of the bandgap; emergence of midgap states; increased of water adsorption energy around defect places; desorption of S atoms and decomposition of FePS ₃ above 500° C into amorphous phase (FeP/FeP ₂ alloyed with S)	[67]
	Co-doped FePS ₃	Experiment/ theory	Increased surface conductivity of MPX3; increased stability towards electrocatalytic OER	[136]
M-vacancy	MnPS ₃	Experiment	Weak ferromagnetism (Note: most probably due to the ion-exchange mechanism during samples' preparation)	[65]
Adsorption				
H ₂ O	$MnPX_3$	Theory	Water splitting is possible at defects; magnetic state is unchanged	[76]
	NiPX ₃	Theory	Molecular adsorption; magnetic state is unchanged	[60]
	CrPX ₃	Theory	Molecular adsorption; magnetic state is unchanged	[61]
	FePX₃	Experiment/ theory	Increased of the water adsorption energy around defect places; low temperature and low partial pressure of H $_2$: physisorption of H $_2$ O on FePX $_3$; high temperature and high partial pressure of H $_2$ O: oxydation of the top FePX $_3$ layer and formation of a P $_x$ O $_y$ "dead" layer.	[67]
NH ₃ , H ₂ , CO, CO ₂ , C ₂ H ₂ , H ₂ S, CH ₄	MnPS ₃	Theory	Weak interaction; no significant effect on magnetic properties	[31,80,81]
NO ₂	$MnPX_3$	Experiment	High sensitivity for NO ₂ adsorption	[78,79]
NO ₂	MnPS ₃	Theory	High sensitivity for NO_2 adsorption; strong adsorption of NO_2 with formation of the P—O bond between molecule and $MnPS_3$	[80]
NO ₂	$MnPS_3$	Theory	Strong interaction; no significant effect on magnetic properties	[81]
NO	MnPS₃	Theory	Strong interaction; substantial enhancement of the exchange interaction between Mn ²⁺ ions; substantial increase in the magnetocrystalline anisotropy energy; induction of intralayer Dzyaloshinskii–Moriya interactions	[81]
CO ₂	FePS ₃	Experiment/ theory	Surprisingly high adsorption energy of CO_2 on $FePS_3$ ($-2.2eV$) in the DFT calculations; spectroscopy and DFT studies on conversion of CO_2 to CH_3OH and C_2H_5OH	[70]
Li, F	MnPX ₃	Theory	Tuning the magnetic state of the top layers; emergence of a HMF state	[83,84]
FM Co-film	FePS ₃	Experiment	Magnetic exchange coupling at the interface; magnetic moments of Fe ions in ${\rm FePS_3}$ are aligned parallel to the magnetization of the Co thin film	[85]
Intercalation				
Li, Na, K	FePS ₃ CoPS ₃ NiPS ₃	Experiment	A redox-type intercalation with reduction of the host lattice	[89,97,99-103]
	MnPS ₃	Experiment	A nonredox process with simple cation exchange without significant changes in the oxidation state of the transition metal	[89,96,97,107-11
Li, Na	NiPS ₃	Experiment	Li intercalation ($x < 0.5$ of Li per NiPS $_4$ f.u.): an anionic redox mechanism in which Ni remains redox-inactive; Li intercalation ($x > 0.5$ of Li per NiPS $_4$ f.u.): decomposition of NiPS $_3$ with formation of Li $_4$ P $_2$ S $_6$ and Li $_2$	[106]
Li	NiPS ₃	Experiment	Electrochemical Li intercalation; ferrimagnetic state for intercalated	[120]

26884046, 0, Downloaded from https://onlinelibrary.wiley.com/doi/10.1002/smsc.20230307 by Ruder Boskovic Institute, Wiley Online Library on (99/10/2023], See the Terms and Conditions, (https://onlinelibrary.wiley.com/terms-and-conditions) on Wiley Online Library for rules of use; OA articles are governed by the applicable Creative Commons License



Table 1. Continued.

Modification	MPX ₃ material	Study approach	Result of modification	References
Li, Na	HEA FeMnNiVZnPS ₃	Experiment/ theory	Aperiodic stacking in HEA and strain soliton boundaries promote the $\mbox{Na}^+\mbox{-}\mbox{ion}$ diffusion	[33]
Li	FePS ₃	Theory	Emergence of a HMF state in intercalation compound	[137]
Li	FePS ₃	Experiment	Electrochemical Li intercalation; FM-like state for intercalated compound with $\mathcal{T}_{\mathcal{C}}$ depending on Li concentration	[138]
Li(K) and NH ₃ co- intercalation	FePS ₃	Experiment	Suppression of the AFM state in intercalation compounds; observation of spin-glass state (at $<50\mbox{K})$	[139]
C ₆ H ₁₁ N ₂ BF ₄ ionic liquid	FePS ₃ NiPS ₃	Experiment	Electrochemical interacalation of ionic liquid; no FM state; after intercalation: unaffected T_N for NiPS $_3$ and reduced T_N for FePS $_3$	[140]
$\label{eq:masses} \begin{split} [M(\text{salen})]^+, \ M &= \text{Mn}^{3+}, \\ \text{Fe}^{3+}, \ \text{Co}^{3+} \end{split}$	MnPS ₃	Experiment	lon-exchange mechanism for intercalation; formation of Mn-vacancies in intercalation compounds; observation of spontaneous magnetization for ${\rm [Fe(salen)]}^+ \ {\rm and} \ {\rm [Mn(salen)]}^+ \ {\rm with} \ {\it T}_C \approx 35 \ {\rm K}$	[115]
TBA ⁺ -cations	NiPS ₃	Experiment	Ferrimagnetic state for the intercalation compound with $T_{\rm C} \approx 78$ K, hysteretic behavior with finite remanence and coercivity	[121]
THA ⁺ -cations	NiPS ₃	Experiment/ theory	Ferrimagnetic state for the intercalation compound with $T_C \approx 100$ K, hysteretic behavior with large remanent magnetization and coercivity	[122]
$Co(Cp)_2^+$ -cations	NiPS ₃	Experiment	Ferrimagnetic state for the intercalation compound with $T_{C} \approx$ 98 K, hysteretic behavior with finite remanence and coercivity	[121]
$Co(Cp)_2^+$ -cations	FePS ₃	Experiment	Ferrimagnetic state for the intercalation compound with $T_{\rm C} <$ 100 K, hysteretic behavior with finite remanence and coercivity	[141]
PyH ⁺ -cations	FePS ₃	Experiment	FM state for the intercalation compound with $T_C \approx 87$ K, hysteretic behavior with finite remanence and coercivity; out-of-plane magnetic anisotropy	[123]
TMA ⁺ -, TEA ⁺ -, TBA ⁺ , CTA ⁺ -cations	MnPS ₃	Experiment/ theory	Nonredox ion-exchange intercalation; formation of Mn-vacancies in intercalation compounds; FM state for the intercalation compound with $T_C \approx 40-60$ K, hysteretic behavior with finite remanence and coercivity and large magnetic moment for Mn ²⁺ ions	[124]

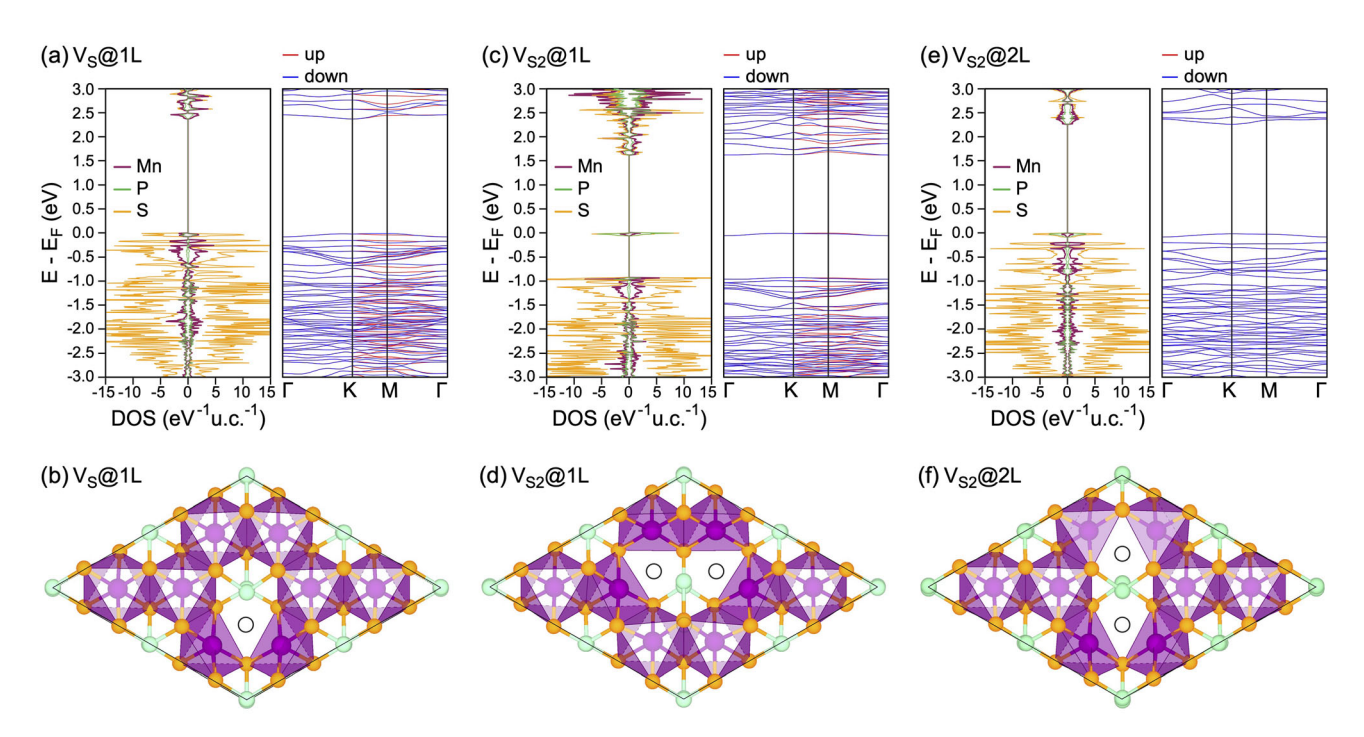


Figure 4. a,c,e) Atom-projected DOS and band structures for defected MnPS₃ single layers with single and double S-vacancies with the corresponding structures presented in (b,d,f), respectively. Reproduced under the terms of the Creative Commons Attribution-NonCommercial 3.0 Unported license.^[37] Copyright 2020, The Authors. Published by The Royal Society of Chemistry.

www.advancedsciencenews.com www.small-science-iournal.com



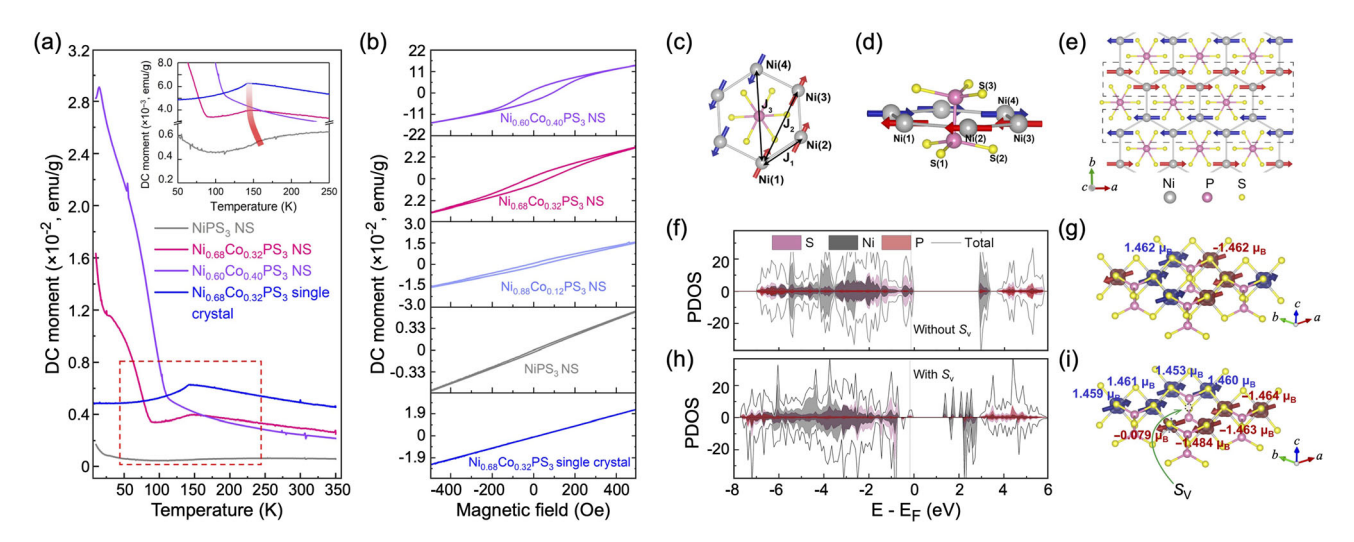


Figure 5. a) Temperature dependence of the zero-field cooled (ZFC) magnetization measured at H = 200 Oe on various $Ni_{1-x}Co_xPS_3$ nanosheets (x = 0, 0.32, 0.40) and the $Ni_{0.68}Co_{0.32}PS_3$ single crystal. b) M - H curves measured at 5 K of various $Ni_{1-x}Co_xPS_3$ nanosheets (x = 0, 0.12, 0.32, 0.40) in comparison with that of the $Ni_{0.68}Co_{0.32}PS_3$ single crystal. c,d) The illustrations of the exchange interactions in a hexagonally arranged lattice of Ni neighbors in NiPS₃ mediated via S atoms. e) Top view of a NiPS₃ ML with alternating FM chains marked with dashed black boxes, coupled antiferromagnetically throughout the crystal lattice. f,h) Spin-polarized atom-projected DOS and g,i) the corresponding illustrations of the magnetic moment distribution of AFM NiPS₃ without S vacancy and with S vacancy. Reproduced under the terms of the Creative Commons Attribution NonCommercial license 4.0 (CC BY-NC). [66] Copyright 2021, The Authors. Published by The American Association for the Advancement of Science.

antiferromagnetically coupled sublattices leads to the prevailing of FM interaction over the AFM correlations at low temperatures.

As discussed earlier, the irradiation of MPX3 materials with a high-energy electron beam can lead to changes in the materials' stoichiometry and, as later found, to the restructuring of trichalcogenides into new materials with different crystallographic structures. Such experiments show that in the case of MnPS₃, the electron beam irradiation leads to a transformation into cubic α-MnS alloyed with P,^[63] whereas for MnPSe₃, the formation of mixed cubic α -MnSe and hexagonal γ -MnSe phases is observed^[64] (Figure 6). Additionally, the thermal stability experiments for these materials show that both MnPX3 materials are converted under vacuum conditions upon thermal annealing into cubic α -MnS/MnSe phases at 490°C/400°C, respectively. Similar thermal stability experiments performed on FePS₃ showed different results^[67] (Figure 7). In this case, bulk FePS₃ crystals were annealed in ultrahigh vacuum conditions, and the so-called "live" X-ray photoelectron spectra (XPS) of the respective core levels were acquired. In contrast to MnPX₃, in the case of FePS₃, the predominant desorption of S atoms is observed, and above 500 °C, this material decomposes into a new amorphous phase consisting of iron phosphides FeP/ FeP₂ alloyed with S, as demonstrated by XPS data. [67]

3.2. Adsorption of Different Species

With the recent progress in the studies of 2D and vdW materials, MPX₃ materials, as wide-bandgap materials, have attracted much attention due to the possibility of using them in water-splitting reactions for hydrogen evolution and oxygen evolution reactions (HER and OER),^[68,69] as well as for CO₂ gas conversion into methanol and/or ethanol.^[70] It has been shown that most of these materials ideally combine the width of the bandgap and

the positions of the bands' edges with respect to redox potentials at different pH values, along with relatively high mobility for electrons and holes.^[71] Many experimental and theoretical works have been devoted to these studies, ^[72–75] yet a systematic approach for considering the adsorption of different species on the surface of MPX₃ has been lacking, raising many controversies and critical questions regarding the interpretation of structural, spectroscopic, and electrochemical data. Thus, later, a series of works were dedicated to analyzing water adsorption on both pristine and defective MPX₃, with a deeper understanding of the possible mechanisms that might govern the effective HER and OER on these materials.

The adsorption of H₂O molecules on the surface of pristine MPX₃ materials is always a physisorption process, with the adsorption energy not exceeding -210 meV per molecule. [60,61,67,76] Only the formation of chalcogen vacancies, which are the most probable defects in the MPX3 layer, leads to a drastic increase in adsorption energy. For example, the adsorption energy is -572 meV per H₂O molecule for a single S-vacancy in NiPS₃^[60] and -1279 meV per H₂O molecule for a double S-vacancy in MnPS₃^[76] (**Figure 8**). The dissociative adsorption of H₂O, when it is split into H⁺ and OH⁻ fragments, is not always energetically favorable, demonstrating either positive adsorption energies (as observed for ideal NiPX3 and MnPX3 surfaces [60,76]) or yielding adsorption energies smaller than those for nondissociative water adsorption (as observed for defective NiPX₃ and CrPX₃^[60,61]). In the case of MnPX₃, it has been found that for all X-defective MnPX3 surfaces, the adsorption energy for H₂O molecules is higher compared to the pristine surface.^[76] Additionally, the energies for dissociative adsorption of H2O on the defective MnPX₃ surfaces become comparable with those for nondissociative adsorption, demonstrating the possibility of implementing HER on this material. In the same study, [76] the

and Conditions (https://onlinelibrary.wiley.com/terms-and-conditions) on Wiley Online Library for rules of use; OA articles are governed by the applicable Creative Commons License

www.advancedsciencenews.com

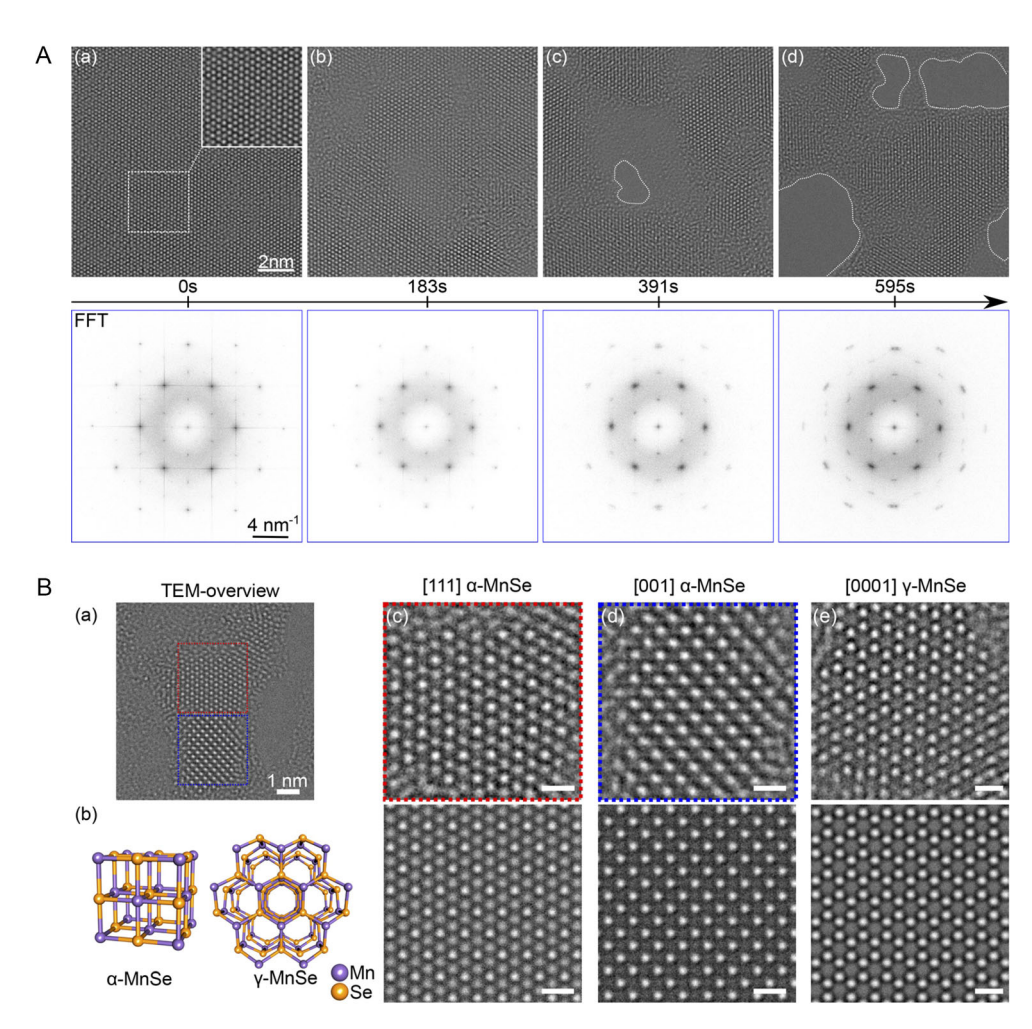


Figure 6. A): a–d) 80 kV Cc/Cs-corrected high-resolution TEM (HRTEM) image series of few-layer MnPSe₃ acquired with a dose rate of $0.6 \times 10^6 \frac{e}{nm^2}$ illustrating the degradation process under electron beam irradiation. Underneath each HRTEM image, the corresponding FFT image is shown. Damage caused by the e-beam irradiation can be observed in the images, and the formation of holes is indicated by the white dotted lines. B): a) TEM overview image of an irradiated MnPSe₃ crystal proofing the emergence of new phases highlighted by dotted boxes; b) model of the emerging phases, namely, of cubic α-MnSe ($Fm\overline{3}m$) and hexagonal γ-MnSe ($P6_3mc$); c–e) HRTEM images of experimentally observed MnSe patches in different orientations and types. Corresponding simulations are given beneath the experimental images. The scale bars in image panels (c–e) represent a length of 0.5 nm. Reproduced with permission. [64] Copyright 2023, American Chemical Society.

Gibbs free energies of the intermediate state, $|\Delta G_{H^*}|$, for different MnPX₃ surfaces (both pristine and defective) were calculated and compared with $|\Delta G_{H^*}| = 0.09$ eV for the well-known highly efficient Pt catalyst. Among all possible configurations, the surface with double X-vacancies demonstrated the lowest values of $|\Delta G_{H^*}| = 0.69$ eV/0.41 eV for X = S/Se, [76] respectively, which are comparable with the corresponding experimental values found in the range between 0.525 and 0.835 eV. [21,77]

A similar behavior is observed for FePX3 materials, where the creation of single X-vacancies in the top FePX3 layer leads to an increase in the adsorption energy of water to $-712/-715 \ meV$ per H_2O molecule, compared to $-209/-207 \ meV$ for X=S/Se, respectively. $^{[67]}$ This molecular adsorption is slightly more energetically favorable than the dissociative adsorption of water molecules on defective FePSe3-x, which exhibits a slightly lower adsorption energy of $-649 \ meV$ per H_2O molecule. These theoretical predictions are supported by corresponding XPS and

NEXAFS (near-edge X-ray absorption fine structure) studies on water adsorption on FePX₃ under ultrahigh vacuum conditions, confirming the physisorption nature of the $\rm H_2O-FePX_3$ interaction in the temperature range of $100-300\,\rm K$ and under low $\rm H_2O$ partial pressures. [67] Additional XPS/NEXAFS measurements at elevated temperatures (above 573 K) and higher water partial pressures (above 0.1 mbar) reveal two competing processes: adsorption at high $\rm H_2O$ partial pressure and desorption due to increased surface mobility and the physisorptive nature of the interaction. Further heating of FePX₃ to 673 K results in partial oxidation of the top layer, leading to the formation of a $\rm P_xO_y$ "dead" layer.

The experimentally observed high gas selectivity of MnPX₃ towards NO₂ under ambient conditions^[78,79] was recently analyzed using DFT calculations.^[80] Theoretical results show that the adsorption energy for various molecules (NH₃, H₂, CO, CO₂, C₂H₂, H₂S, CH₄) does not exceed -160 meV per adsorbed

26884046, 0, Downloaded from https://onlinelibrary.wiley.com/doi/10.1002/smsc.202500307 by Ruder Boskovic Institute, Wiley Online Library on [09/102025]. See the Terms and Conditions (https://onlinelibrary.wiley.com/erms

and-conditions) on Wiley Online Library for rules of use; OA articles are governed by the applicable Creative Commons License

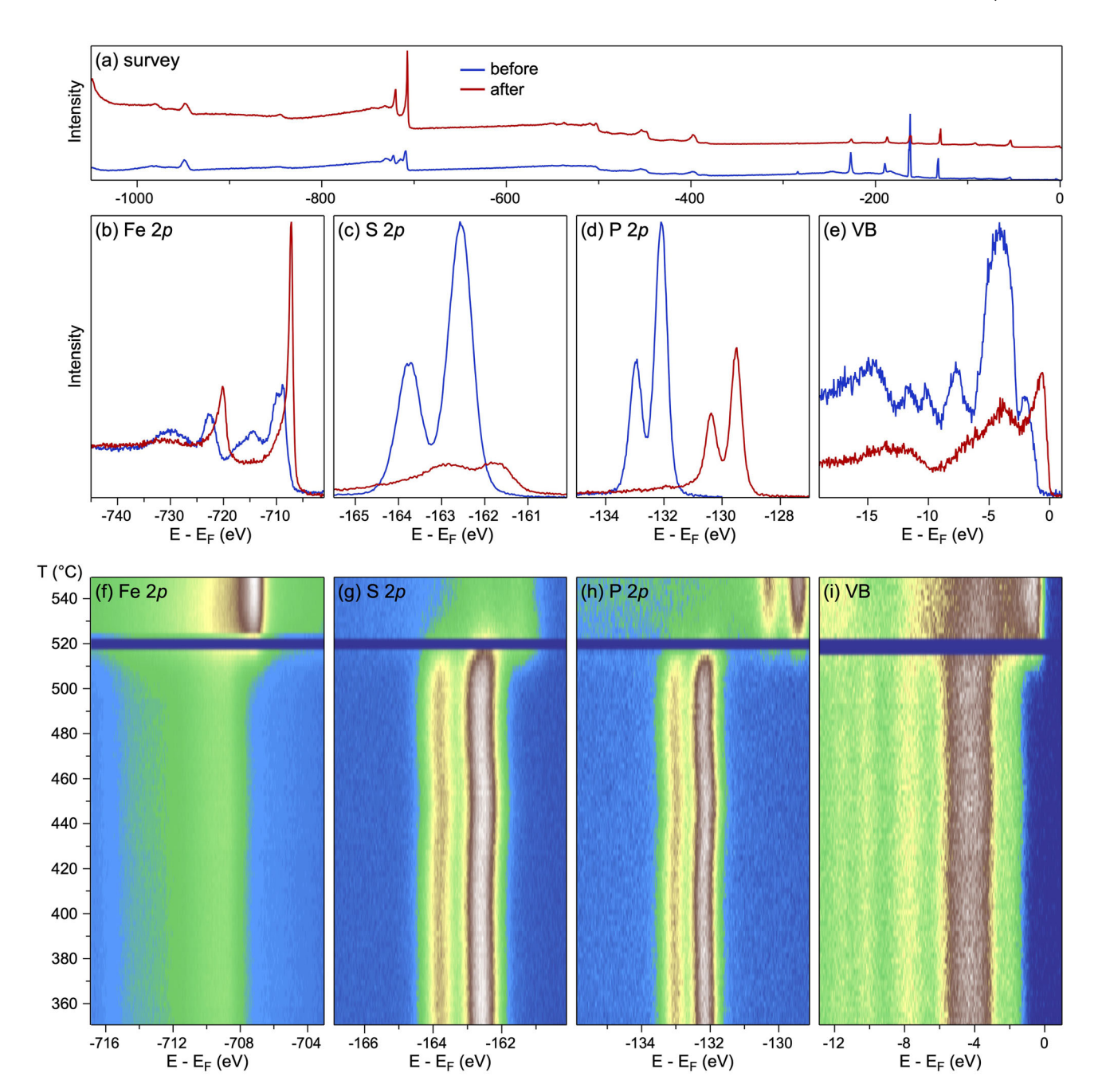


Figure 7. XPS spectra (measured at room temperature) collected for FePS₃ before and after temperature stability experiments: a) survey, b) Fe 2p, c) S 2p, d) P 2p, and e) valence band. f–i) Photoemission intensity maps based on the sequences of the respective XPS spectra collected in the "snapshot" mode of the analyzer as a function of the sample temperature. Spectra are shown in the temperature range of 350 – 550°C. The temperature gradient is 3 degrees per minute. All spectra were collected at photon energy of $h\nu = 1000$ eV. Horizontal intensity drops in (f–i) are due to the closed last valve of the beamline when pressure in the chamber raised above the working limit. Reproduced with permission. [67] Copyright 2023, IOP Publishing.

molecule. In contrast, NO_2 molecules adsorb on MnPS $_3$ with a much higher energy of $-640\,\text{meV}$ per NO_2 molecule. Upon adsorption, one of the N–O bonds in NO_2 breaks, and a P–O bond forms between NO_2 and MnPS $_3$. Furthermore, a significant increase in the density of states (DOS) occurs near the Fermi level, resulting in a pronounced change in the electrical conductivity of MnPS $_3$ and a high response to NO_2 molecules. [80]

As discussed in Section 2, the NN magnetic coupling in MPX₃ materials can be tuned through various mechanisms. One particularly promising approach involves enhancing the M–X–M superexchange interaction to surpass the direct M–M exchange in determining the J_1 coupling parameter. The influence of molecular adsorption on the magnetic properties of MnPS₃ was investigated in ref. [81], focusing on several species including CO, N₂, NH₃, NO, and NO₂. In all cases, adsorption was

26884046, 0, Downloaded from https://onlinelibrary.wiley.com/doi/10.1002/smsc.202500307 by Ruder Boskovic Institute, Wiley Online Library on [09/10/2025]. See the Terms and Conditions (https://onlinelibrary.wiley.com/term

and-conditions) on Wiley Online Library for rules of use; OA articles are governed by the applicable Creative Commons License

www.advancedsciencenews.com

www.small-science-iournal.com

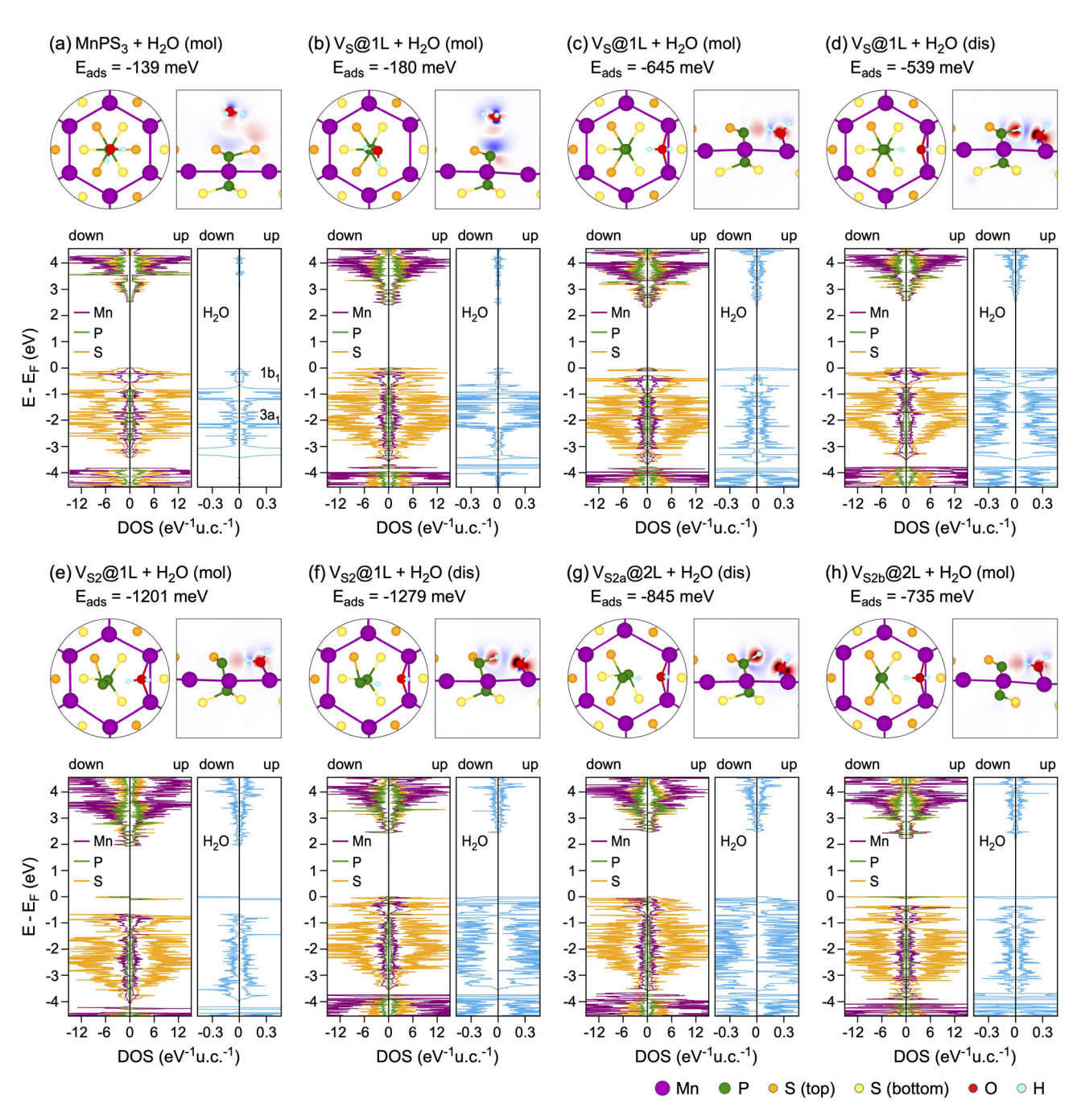


Figure 8. Top and side views of the relaxed structures obtained after water adsorption on pristine and defective MnPS₃. Spheres of different size/color represent ions of different types. Side views are superimposed with electron density redistribution maps: $\Delta \rho(r) = \rho_{A/B}(r) - [\rho_A(r) + \rho_B(r)]$ (A: adsorbate; B: substrate). Here, $\Delta \rho(r)$ is color-coded as blue (-0.01 eÅ^{-3}) —white (0)—red $(+0.01 \text{ eÅ}^{-3})$ in (a,b) and as blue (-0.1 eÅ^{-3}) —white (0)—red $(+0.1 \text{ eÅ}^{-3})$ in (c-h). Bottom part of each panel presents the atom-projected DOS obtained with PBE + U + D2 for the respective structures. Reproduced with permission. [76] Copyright 2023, American Chemical Society.

characterized as physisorption, with adsorption energies ranging from \approx -100 to -200 meV per molecule for CO, N₂, and NH₃, which are similar to previous works. In contrast, significantly stronger adsorption was observed for NO and NO2, with energies of -446 and -492 meV, respectively. These values are lower by pprox150 meV compared to those previously reported in ref. [80] for the adsorption of NO and NO2, which can be attributed to slightly different computational settings used in these highly sensitive calculations. Further analysis revealed that NO molecules induce the most pronounced changes in the magnetic properties of the MnPS₃ layer, resulting in a substantial enhancement of the exchange interaction between Mn²⁺ ions. This effect is attributed to the emergence of a new exchange pathway mediated by the NO molecules, which surpasses the conventional Mn-S-Mn

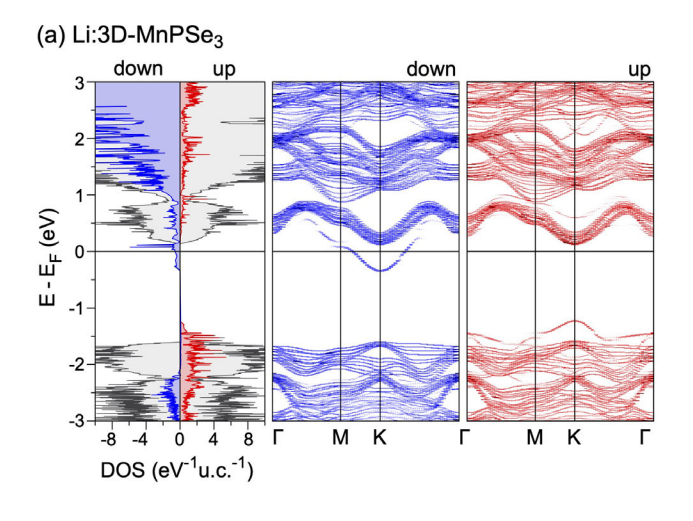
www.small-science-iournal.com

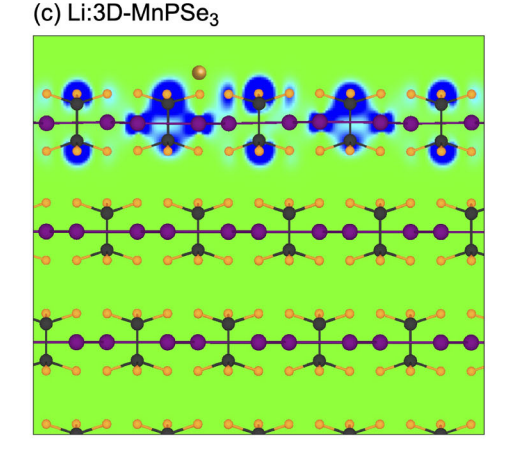
superexchange interaction. Additionally, NO adsorption leads to a substantial increase in the magnetocrystalline anisotropy energy and induces intralayer Dzyaloshinskii–Moriya interactions. As was shown, these effects are likely a consequence of lattice distortions in MnPS₃ following NO adsorption.

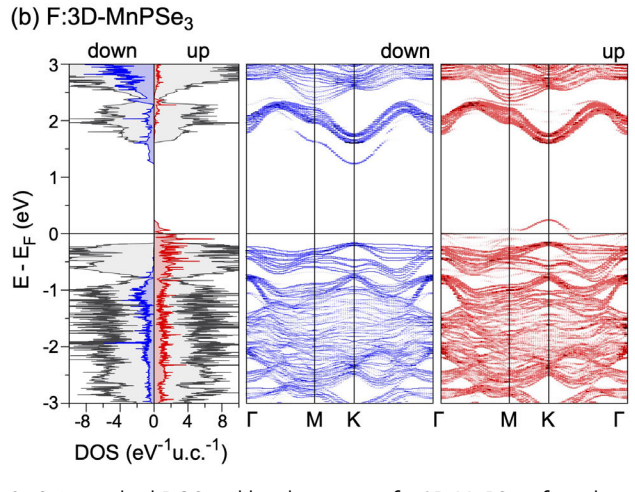
A more effective strategy for modifying the magnetic properties of MPX₃ through adsorption is inspired by studies on doping MnPSe₃ layers using an external electric field.^[82] It was demonstrated that both electron and hole doping can be experimentally realized at feasible carrier concentrations, leading to the emergence of a half-metallic ferromagnetic (HMF) state.

Building on the concept of doping or charge transfer in MPX₃-based systems, a study investigating the adsorption of Li and F atoms on stacked MnPX₃ layers demonstrated that a HMF state can be realized selectively in the topmost MnPX₃ layer, while the underlying bulk-like layers remain largely unaffected^[83] (**Figure 9**). Remarkably, tuning the magnetic state of the top layers of both MnPX₃ compounds can be achieved with as little as 0.25 monolayers (MLs) of adsorbed guest atoms. Specifically,

MnPS3 transitions to an HMF state upon Li adsorption, but retains its AFM character in the presence of F. In contrast, MnPSe₃ exhibits an HMF state upon adsorption of either Li or F. It was found that Li atoms preferentially adsorb above Mn sites, while F atoms favor adsorption above P atoms. In all cases, charge redistribution occurs in the top MnPX3 layer: Li adsorption leads to charge accumulation on Mn—S/Se bonds, whereas F adsorption results in charge accumulation primarily on S or Se atoms. This redistribution modifies the magnetic exchange interactions, particularly enhancing the superexchange Mn-S-Mn interaction upon Li adsorption, thereby increasing the magnitude and altering the sign of all I values. As a result, the HMF state emerges, with Curie temperatures of $T_C = 198$ and 126 K for MnPS₃ and MnPSe₃, respectively. F adsorption is less effective, yielding an HMF state only in MnPSe₃, where the NN exchange (I_1) becomes negligible and the magnetic coupling is dominated by the 3NN interaction (I_3), leading to a Curie temperature of $T_C = 85$ K. Due to the vdW nature of interlayer interactions in MnPX3, even with substantial electron or hole







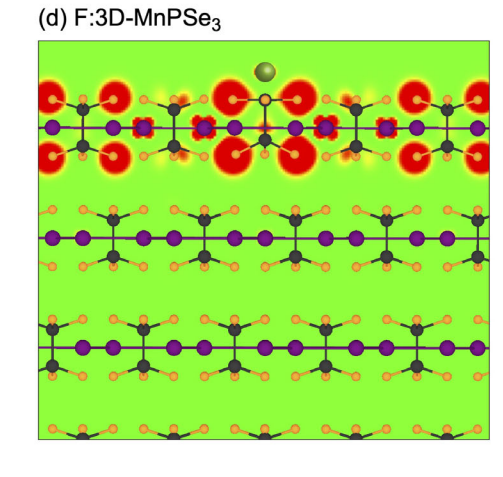


Figure 9. Spin-resolved DOS and band structures for 3D MnPSe₃ after adsorption of Li a) (Li:3D-MnPSe₃) and F b) (F:3D-MnPSe₃). In DOS plots, the grey shaded areas indicate the total DOS and the blue/red shaded areas indicate the spin-down/spin-up DOS projected onto the atoms of the outermost MnPSe₃ layers. c,d) The real-space spin-density distribution maps overlaid with the respective structures for Li:3D-MnPSe₃ and F:3D-MnPSe₃, respectively. The maps are color-coded as blue $(-0.001 \, \text{eÅ}^{-3})$, green (0), and red $(+0.001 \, \text{eÅ}^{-3})$. Reproduced with permission. (83) Copyright 2022, The Royal Society of Chemistry.

www.small-science-iournal.com

www.small-science-journal.com

doping of the topmost layer, the inner layers remain in an AFM state with a wide bandgap. As proposed in ref. [83], such a configuration could be harnessed to construct an electric-field-driven "one-material"-based magnetic tunnel junction. This setup would feature ideal interfaces between conductive and insulating layers, minimizing electron scattering and improving performance in potential spintronic devices. These theoretical predictions were later supported in ref. [84], where it was also suggested that an HMF state in MnPS₃ can be induced by adsorption on a metallic substrate such as Au(111). This phenomenon obtained theoretically for MnPS₃ may be taken as another mechanism for the previously experimentally observed "parasitic" ferromagnetism in few-layer MnPS₃. [65]

A more straightforward approach to modifying the magnetic state of MPX₃ materials involves the adsorption of thin ferromagnetic layers. However, only a limited number of studies on this topic are available in the literature. In ref. [85], a relatively thick Co film (≈7 nm) was deposited onto FePS₃, and the magnetic properties of the resulting interface were investigated using magneto-optical Kerr effect microscopy and X-ray magnetic circular dichroism (XMCD). The Co film exhibited isotropic magnetic behavior, suggesting the absence of a preferred magnetic anisotropy direction. This was attributed to the lack of layer-by-layer growth during deposition, likely caused by the significant surface energy mismatch between Co and FePS₃. Low-temperature magnetic measurements revealed no clear exchange bias in the FM-Co/AFM-FePS3 system. However, a sharp reduction in coercivity was observed above 110 - 120 K, near the Néel temperature of FePS3, indicating the presence of exchange coupling at the interface. Unfortunately, no low-temperature XMCD data were provided for the Co/FePS3 system, and only room-temperature spectroscopic measurements, conducted well above the T_N of FePS₃, were reported. From the NEXAFS and XMCD spectra at the Fe $L_{2,3}$ absorption edges, a mixed Fe²⁺/Fe³⁺ signal was detected in the Co/FePS₃ sample, in contrast to the purely Fe²⁺ signal observed in pristine FePS₃.^[49] Control experiments confirmed that the appearance of Fe³⁺ is linked to the formation of the Co/FePS₃ interface, corroborating previous observations in Co- and Ni-doped FePS3 systems. [86,87] These results also indicate that magnetic exchange coupling occurs at the interface between FM Co and paramagnetic (at room temperature) FePS₃, as evidenced by the dichroic signal observed at the Fe $L_{2,3}$ edges. The magnetic moments of Fe ions were found to align parallel to the magnetization of the Co thin film. Nevertheless, further experimental and theoretical investigations are required to elucidate the nature of this magnetic proximity effect, including the observed reorientation of FePS₃ magnetic moments from out-of-plane to in-plane alignment.

3.3. Intercalation of Different Species

The discussed MPX₃ materials, as representative examples of layered compounds, are well suited for modification via intercalation—a widely used technique in which guest species are inserted into the available voids of the host material. In the case of MPX₃, a natural intercalation pathway involves the insertion of guest atoms or molecules into the interlayer regions,

which are initially held together by weak vdW forces. This approach enables significant tuning of the material's electronic and magnetic properties without disrupting the in-plane atomic structure.

As previously discussed in the literature, [88,89] several well-established methods exist for the intercalation of layered materials. These include direct thermal reactions between the host lattice and guest species, indirect reactions involving auxiliary processes that provide a net gain in free enthalpy, electrochemical intercalation using an appropriate electrolytic cell with the host lattice as the cathode, and ion-exchange reactions. In general, intercalation leads to charge transfer between the guest species and the host lattice, which can profoundly affect the electronic, optical, and magnetic properties of the parent compound. Additionally, intercalation typically results in an expansion of the interlayer spacing (i.e., an increase in the lattice parameter c). These structural and electronic changes may also give rise to further modifications, such as alterations in stacking order, increased structural disorder, and the formation of distinct intercalation stages. During the 1970s-1990s, numerous experimental studies explored the intercalation of MPX3 materials with a wide range of guest species—from small alkali metals like lithium to larger organic molecules such as cobaltocene ($Co(C_5H_5)_2$) and pyridine. [57,90-93] In the present work, we focus on more recent efforts aimed at achieving two primary objectives through intercalation in MPX3 systems: 1) their application as electrode materials in rechargeable batteries and 2) the tuning of their magnetic ordering.

Extensive research has been devoted to understanding the mechanism of lithium intercalation in various MPX₃ compounds. [89,94-96] It was found that the reaction of these materials with *n*-butyl-lithium, commonly used as the main agent in electrochemical intercalation, proceeds differently depending on the specific transition metal involved. These differences have been attributed to the electronic configuration of the M²⁺ ions, particularly the occupancy of their 3d orbitals. For instance, FePS₃, CoPS₃, and NiPS₃, which have partially filled 3d shells, undergo rapid intercalation with n-butyl-lithium. In contrast, MnPS₃, with a half-filled $3d^5$ configuration, requires significantly longer reaction times—often several weeks—to achieve noticeable Li intercalation. [89,97] Based on these findings, two distinct intercalation mechanisms have been proposed for MPX3 compounds: 1) a redox-type intercalation, involving reduction of the host lattice (as observed in FePS3, CoPS3, and NiPS3) and 2) a nonredox process, characterized by simple cation exchange without significant changes in the oxidation state of the transition metal (as in the case of MnPS3 and CdPS3).[89,96,98]

The reduction of the host lattice during lithium intercalation in NiPS $_3$ has been investigated in several studies using various spectroscopic techniques. Early evidence was provided by nuclear magnetic resonance (NMR) and Mössbauer spectroscopy, [99,100] and was later revisited using Raman spectroscopy and extended X-ray absorption fine structure analysis. [101–103] More direct confirmation of the reduction of Ni²⁺ ions to metallic Ni⁰ upon Li intercalation was obtained through XPS. [96] A comparison of the XPS spectra for pristine NiPS $_3$ and Li $_x$ NiPS $_3$ reveals notable shifts in the core-level binding energies: the Ni 2p and 3p peaks shift to lower binding energies in the intercalated compound,

while the P 2p peak shifts to higher binding energy. After intercalation, the Ni emission lines approach those characteristic of metallic nickel, and the satellite features typically present in the Ni 2p spectrum of Ni²⁺ (refs. [104,105]) are significantly suppressed. These spectral changes provide compelling evidence for the reduction of Ni²⁺ ions to Ni⁰, strongly supporting the redox intercalation model in NiPS₃.

Recent structural and spectroscopic investigations of Li and Na intercalation in NiPS₃ have provided new insights into the intercalation mechanism and its electronic consequences^[106] (**Figure 10**). These studies show that, during the initial stages of intercalation, up to \approx 0.5 Li or Na ions per NiPS₃ formula unit can be accommodated within the free octahedral sites located between the vdW-bonded layers. Surprisingly, systematic in

operando X-ray absorption spectroscopy (XAS) measurements at the Ni K-edge revealed minimal spectral changes over the range $0 \le x \le 1$, indicating that Ni remains largely unaffected during this phase of Li insertion (see Figure 10a). A similar lack of significant spectral variation was also observed during Na intercalation (see Figure 10b). In contrast, clear modifications were detected at the P K- and S K-edges, suggesting that the electron density is redistributed primarily on the $(P_2S_6)^{4-}$ polyanion unit (see Figure 10c,d). From these observations, it was concluded that Li intercalation proceeds via an anionic redox mechanism in which Ni remains redox-inactive. Conversely, Na intercalation induces a reduction of Ni, highlighting a cation-specific intercalation behavior. Moreover, intercalation beyond 0.5 Li per NiPS3 formula unit leads to the formation

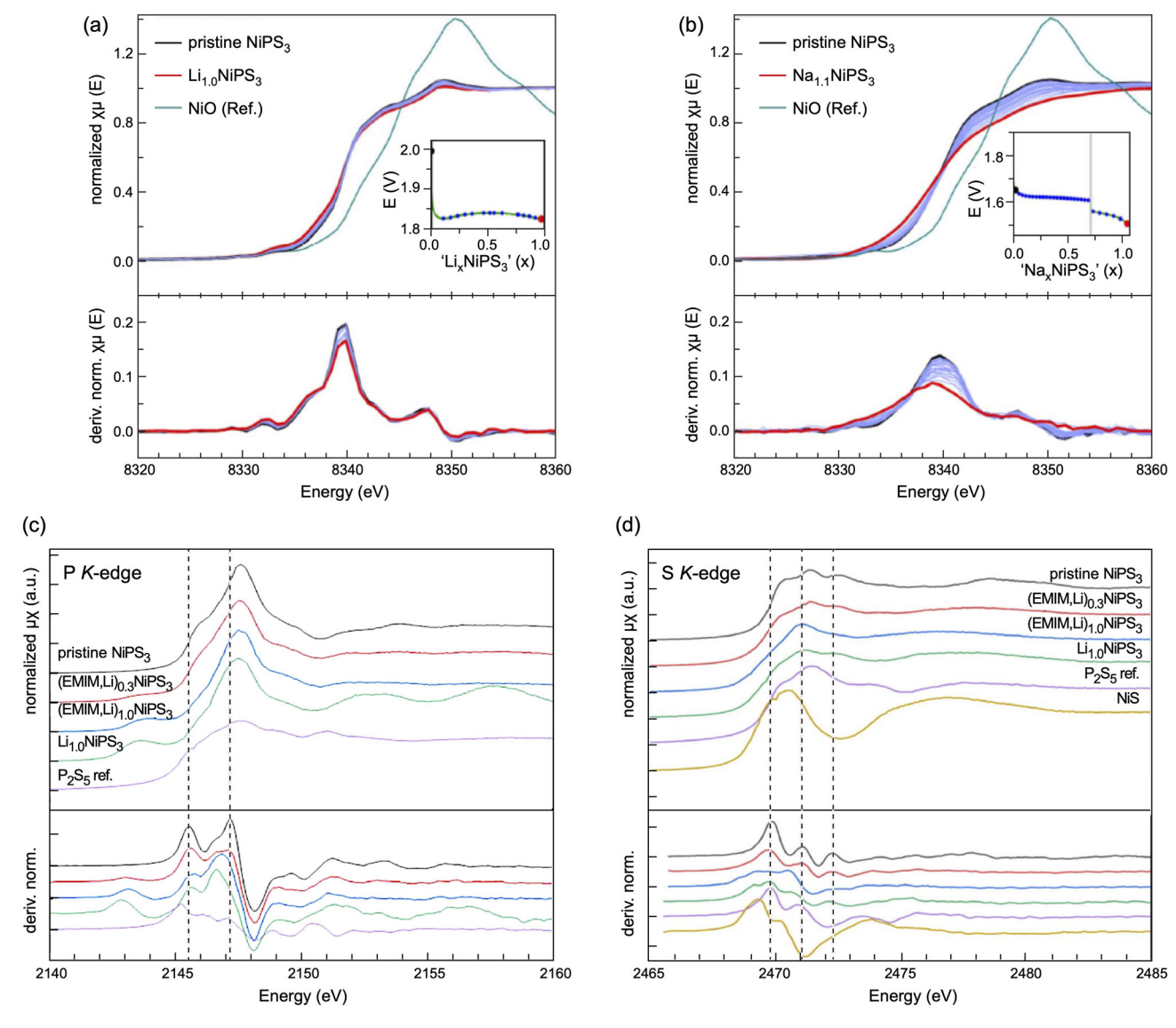


Figure 10. Operando XAS spectra of alkali ion intercalation into NiPS₃: a) Ni K-edge and $d\mu(E)/dE$ plots of Li_xNiPS₃ ($0 \le x \le 1$), b) Ni K-edge and $d\mu(E)/dE$ plots of Na_xNiPS₃ ($0 \le x \le 1$). Insets show the corresponding potential profiles and the specific points of measurement. Ex situ XAS data: c) P K-edge of pristine, EMIM and Li co-intercalated NiPS₃ and a P₂S₅ reference material including the first derivative of the normalized absorption coefficient, d) S K-edge of pristine, EMIM and Li co-intercalated NiPS₃ and a P₂S₅ reference material including the first derivative of the normalized absorption coefficient. Reproduced with permission.^[106] Copyright 2024, The Royal Society of Chemistry.

www.small-science-iournal.com

of decomposition products, including Li₄P₂S₆ as an intermediate and Li₂S as the final product of lithiation.

In contrast to the electron transfer and host lattice reduction observed in NiPS₃, the intercalation of Li, Na, and K into MnPS₃ proceeds via ion transfer—specifically, a cation exchange mechanism between the guest ions and Mn²⁺ in the host lattice. This process results in the formation of Li(Na)(K)_{2x}Mn_{1-x}PS₃ solid solutions.[107–110] The intercalation can be achieved through a simple soaking and stirring procedure, wherein MnPS3 is exposed to an aqueous LiCl, NaCl, or KCl solution. As found from the X-ray diffraction, such intercalation of Li, Na, and K leads to the increase of the interlayer distance in $Li(Na)(K)_{2x}Mn_{1-x}PS_3$ to c' = 11.9, 11.8, and 9.4 Å, respectively, compared to $c^{'}=6.5\,\mathrm{\AA}$ for the parent MnPS $_3$ compound. [108–110] XPS analysis of both pristine and intercalated compounds reveals no significant shifts in binding energy or changes in the spectral features—including the satellite structures—of the Mn core levels or the valence band. These observations strongly support a cation exchange intercalation mechanism rather than a redox process in MnPS₃.

Recent advancements in the synthesis strategies of MPX₃ materials have enabled the successful fabrication of the (HEAs),[111-114] high-entropy alloys Co_{0.6}(VMnNiZn)_{0.4}PS₃^[34] and FeMnNiVZnPS₃^[33] (high-resolution TEM images of these materials are shown in Figure 3). These materials are being actively explored for various energy-related applications due to their unique structural and electrochemical properties. In the case of FeMnNiVZnPS3, the formation of aperiodic structures was observed throughout the crystals, resulting in a high density of strain soliton boundaries. These boundaries arise from the local stress imbalance caused by the presence of metalsulfur (M-S) bonds of differing lengths and strengths. Theoretically predicted and experimentally confirmed through high-resolution microscopy, these strain soliton boundaries serve as sites for localized electric field enhancement, which significantly promotes ion diffusion. Furthermore, the observed buckling of the vdW layers, in combination with these local electrostatic fields, was found to facilitate the diffusion of Na⁺ ions. The experimentally obtained Na+ diffusion coefficient for FeMnNiVZnPS3 is in the range of $10^{-9.7} - 10^{-8.3}$ cm²s⁻¹, which is higher than the corresponding value of $10^{-10.6} - 10^{-8.3} \text{cm}^2 \text{s}^{-1}$ for FePS₃.^[33] The HEA-based electrodes fabricated from FeMnNiVZnPS3 also exhibit higher capacity of 733.2 mAhg⁻¹ compared to 647.9 mAhg⁻¹ for FePS₃-based electrodes. These experimental findings are supported by the respective theoretical modeling, which indicates a lower energy barrier (by $\approx 0.8 \, \text{eV}$) for the Na⁺-ions diffusion in FeMnNiVZnPS3 compared to FePS3. This insight is critical for the design and optimization of next-generation battery materials based on high-entropy vdW compounds.

Until recently, the magnetic properties of intercalation compounds based on MPX3 materials had not been extensively studied. Only with the emergence of modern theoretical insights into the magnetic exchange mechanisms in MPX3 lattices it has become possible to carry out more targeted investigations of these effects. In one of the earlier studies, the magnetic properties of MnPS₃-based intercalation compounds, with [M(salen)]⁺ complexes (M = Mn^{3+} , Fe^{3+} , Co^{3+} ; salen = NN-ethylene-bis (salicylideneimine)), were examined experimentally. [115] The ion-exchange mechanism characteristic for MnPX3 is also observed in this study, leading to creation of Mn vacancies in the formed intecalation compounds. It was found that the orientation of the intercalated molecules, as well as the resulting expansion of the interlayer vdW spacing, depended on the concentration of the guest species—likely affecting the doping level of individual MnPS₃ layers. As a consequence of this dependence, intercalation with [Fe(salen)]⁺ and [Mn(salen)]⁺ led to the emergence of bulk spontaneous magnetization, with a transition from the paramagnetic to the ferromagnetic state observed at around 35 K. In contrast, intercalation with [Co(salen)]⁺ left the material in a paramagnetic state.

More intensive and systematic studies on the tuning of the magnetic properties of various MPX3 materials were motivated by recent theoretical works, [20,37,82-84,116-119] which provided detailed analyses of their electronic and magnetic structures, along with potential modification strategies. Among the most natural and widely suggested approaches was the intercalation of Li into the MPX3 lattice, where Li acts as an electron donor, thereby tuning the magnetic exchange interactions between the originally antiferromagnetically coupled M²⁺ ions. This strategy was experimentally realized in ref. [120], where Li was electrochemically intercalated into bulk NiPS3, achieving a maximum composition of Li_xNiPS₃ with x = 0.6 per formula unit. A corresponding expansion of the interlayer spacing was observed, confirming Li⁺ ion insertion into octahedral sites within the vdW gaps of NiPS₃. As a result of the intercalation, the system exhibited an FM response at very low temperatures (\approx 2 K), while the original AFM ordering persisted at higher temperatures with a nearly unchanged Néel temperature of $T_N \approx 155$ K. This behavior was attributed to the zigzag AFM structure of the NiPS3 layers, consisting of two magnetic sublattices. Li intercalation introduces an imbalance in the spin-up and spin-down electron populations, rendering the magnetic moments of the two sublattices unequal and thus inducing weak ferromagnetism at low temperatures. This explanation is consistent with the small net magnetic moment of $\approx 10^{-3} \mu B$ per Ni atom observed in the measurements.

Further studies on the intercalation of large molecules into MPX₃ demonstrated the successful intercalation of tetrabutylammonium (TBA⁺) and tetraheptylammonium (THA⁺) cations into NiPS₃ bulk^[121,122] (**Figure 11**A). After intercalating these species, transition temperatures between ferrimagnetic and AFM states were observed at 78 K for TBA⁺ and \approx 100 K for THA⁺, with corresponding magnetic moments of $\approx 0.02 - 0.07 \mu_{\rm B}$ per unit cell. Further analysis revealed the reduction of Ni²⁺ ions to Ni⁰ upon intercalation, leading to a displacement of these atoms from the O_h sites in the NiPS₃ lattice to the T_d sites. This displacement causes a significant change in the magnetic moment of Ni from the highspin state (2.83 $\mu_{\rm B}$) in O_h to a low-spin state (zero magnetic moment) in T_d . In the case of fractional intercalation, such as (TBA)_{0.25}NiPS₃, the AFM order of the parent NiPS₃ lattice is not fully compensated, resulting in ferrimagnetic ordering in the intercalated compound. Theoretical analysis [122] confirmed that at doping levels of 0.2 - 0.5 electrons per unit cell—achieved in the experiments—dopant electrons occupy only one Ni sublattice, leading to interchain spin splitting. This imbalance in the magnetic moments between the two Ni sublattices generates a net magnetic moment and ferrimagnetic ordering in the intercalated NiPS3.

and-conditions) on Wiley Online Library for rules of use; OA articles are governed by the applicable Creative Commons License

*A*DVANCED

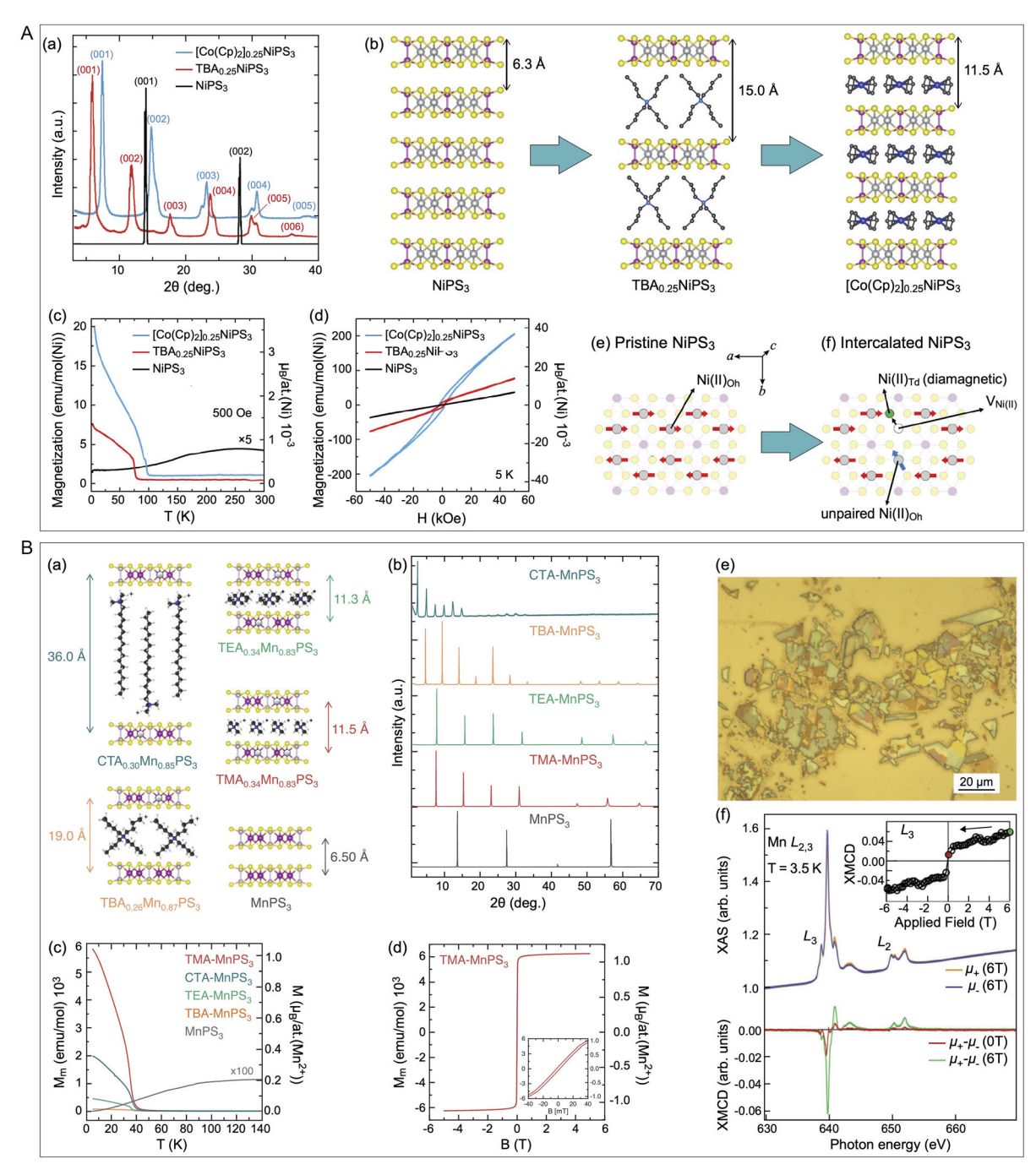


Figure 11. A) Experiments on intercalation of organic ions in bulk NiPS₃: a) XRD patterns of bulk TBA_{0.25}NiPS₃ and [Co(Cp)₂]_{0.25}NiPS₃ in comparison with those of bulk NiPS₃; b) scheme of the intercalation and ion exchange when going from bulk NiPS₃ through TBA_{0.25}NiPS₃ to [Co(Cp)₂]_{0.25}NiPS₃. The respective interlayer distances are marked in the figure; c) field-cooled molar magnetization versus temperature for bulk NiPS₃, TBA_{0.25}NiPS₃, and [Co(Cp)₂]_{0.25}NiPS₃ crystals. The applied field (500 Oe) is oriented parallel to the *ab* plane of the crystal; d) hysteresis loops at 5 K of bulk pristine NiPS₃, TBA_{0.25}NiPS₃, and [Co(Cp)₂]_{0.25}NiPS₃ crystals; e,f) Scheme of the structural change in the NiPS₃ layer accompanying the reduction of the Ni atoms. Reproduced with permission. Copyright 2022, The Royal Society of Chemistry. B) Experiments on intercalation of organic ions in bulk MnPS₃: a) schemes and b) respective XRD patterns of pristine bulk MnPS₃ and four R₄N⁺-MnPS₃ intercalates. The respective interlayer distances are marked in the figure; c) temperature dependence of the magnetization measured for a pristine MnPS₃ crystal and for the four R₄N⁺-MnPS₃ intercalates, under an out-of-plane magnetic field B = 0.1 T. The magnetization of the pristine MnPS₃ crystal has been multiplied by a factor 100; d) hysteresis loop measured with the field applied out of plane for TMA-MnPS₃ intercalate. The inset displays the low field region, characterized by the opening of a magnetic hysteresis; e) optical image of the TMA-MPS₃-intercalated flakes deposited on a gold substrate; f) top: Mn L_{2,3} XAS for right (orange) and left (blue) circularly polarized light measured at 3.5 K and 6 T magnetic field (green) and after field removal (red curve). Reproduced with permission. Copyright 2024, John Wiley and Sons.

www.advancedsciencenews.com www.small-science-journal.com

www.smaii-science-journai.co

Interestingly, the initially intercalated TBA⁺ cations can be replaced by cobaltocene cations (Co(Cp)₂⁺) through an ion-exchange process, yielding a higher transition temperature of 98 K and a larger remanent magnetization^[121] (Figure 11A).

The intercalation of pyridine ions (PyH+) in FePS3 was achieved in ref. [123] using a one-step ion-exchange reaction, where the concentration of the intercalant was controlled by adjusting the temperature and intercalation duration. It was found that PyH⁺ ions can be arranged either parallel or perpendicular to the FePS₃ layers, ultimately influencing the magnetic properties of the system. In both configurations, hard ferromagnetism was observed below a transition temperature of $T_C \approx 87$ K. However, the magnetic response was stronger when the PyH⁺ ions were aligned parallel to the FePS₃ layers, suggesting a larger charge transfer between the guest and host materials in this phase. DFT calculations revealed that the intercalation of PyH⁺ significantly alters the J_n coupling parameters, yielding values of $J_1 = 6.275 \,\text{meV}$, $J_2 = -1.981 \,\text{meV}$, and $J_3 = 2.975$ meV. Along with a large magnetic moment for the Fe sites ($\approx 3.3 - 3.6 \mu_B$) and FM ordering, these changes led to a predicted transition temperature of 35 K. Further experimental investigations ruled out the formation of Fe2+ defects (vacancies), indicating that the observed strong FM order in the PyH⁺intercalated FePS3 is due to pure electron doping.

While the previously discussed works demonstrate the appearance of (ferri)magnetic order in electron-doped FePS3 and NiPS3 obtained through the intercalation of respective cations, a different mechanism for the emergence of magnetism in organic-ionintercalated MnPS₃ was recently discovered^[124] (Figure 11B). Various organic ions, including tetramethylammonium (TMA+), tetraethylammonium (TEA+), tetrabutylammonium (TBA+), and cetyltrimethylammonium (CTA+), were successfully intercalated into MnPS3 via the ion-exchange mechanism, which was previously used for the intercalation of Li and K into MnPS₃. [107,110] This process is nonredox and does not involve charge carrier doping in MnPS₃. The final compositions determined experimentally were: $TMA_{0.34}Mn_{0.83}PS_3$, $TEA_{0.34}Mn_{0.83}PS_3, \ TBA_{0.26}Mn_{0.87}PS_3, \ and \ CTA_{0.30}Mn_{0.85}PS_3.$ All of these intercalation systems clearly exhibit FM ordering at temperatures below $T_C \approx 40 - 60$ K, with the specific transition temperature varying depending on the intercalated species. The largest magnetic moment of $\approx 1.1 \mu_B$ per Mn²⁺ was found for TMA_{0.34}Mn_{0.83}PS₃, accompanied by a very narrow hysteresis loop. Theoretical modeling shows that Mn²⁺ vacancies are arranged within the AFM sublattice of MnPS3 with magnetic moments aligned in the same direction. This creates an imbalance between the two sublattices, leading to the observed magnetic state in the intercalated compound. Further investigation of the TMA-MnPS₃ intercalation compound using XMCD at very low temperatures revealed the presence of magnetic contrast in the remanent state, confirming the existence of an ordered FM state in the studied samples.

4. Conclusions and Outlooks

Layered vdW transition metal phosphorus trichalcogenides (MPX₃) encompass a wide range of elements from the periodic table and can contain M^{2+} and M^{3+} magnetic ions with both

filled and empty *d*-shells. The metal ions are situated in octahedral coordination with chalcogen atoms, and the electronic and magnetic properties of these materials are strongly influenced by the specific M/X combination. In terms of electronic structure and properties, MPX₃ materials exhibit a combination of three types of bonds—ionic, covalent, and vdW—making their property description a complex task, however, allowing for property tunability across a very wide range.

In this review, we provide an overview of the properties of the parent MPX₃ materials and various approaches currently used to modify their electronic, optical, and magnetic characteristics. We also discuss the relationship between structural changes and electronic structure modifications. Among the methods highlighted for modifying the properties of vdW MPX3 materials are defect (vacancy) formation and its impact on material stability, adsorption of different species, and intercalation of various guest ions and molecules. As demonstrated, in many cases, the original properties—such as the wide-bandgap and AFM ground state of the parent compounds—are significantly altered, resulting in new properties. These modifications open up opportunities to apply both the parent and modified MPX₃ materials in areas such as catalysis, sensing, and spintronics. Notably, the most promising applications include using MPX3 in battery technology (for alkali-metal ion storage) and in spintronics, as the AFM ground state can be converted into a FM state through the discussed modification approaches.

Despite significant advancements in the synthesis, modification, and proposed applications of various MPX3 materials and their derivatives, research on these materials—particularly regarding the fundamental approaches to studying their electronic and magnetic properties—remains in its early stages. Some challenges and potential short- to medium-term prospects for MPX3 in various research and application areas can be outlined as follows (Figure 12): 1) After the recent progress in the synthesis of high-quality bulk MPX3 materials, it has become evident that their relatively large bandgaps and poor conductivity limit further studies and applications. One potential solution is the development of high-quality, large-scale ML or multilayer thin films of MPX₃ on various substrates, including insulating, semiconducting, or metallic materials. As mentioned in Section 2, recent methods for synthesizing small ML-thick MPX3 layers (with lateral sizes of $\approx 100 \,\mu\text{m}$) on SiO₂/Si substrates^[58,59] show great potential, although scalability remains a significant challenge. Therefore, further improvements or new developments in this area are highly desirable. 2) The application of alloy engineering to modify and tune the electronic, optical, and magnetic properties of MPX₃ materials is still limited and requires more systematic studies. Several directions can be considered: a) Doping of parent MPX₃ compounds: Introducing small amounts of guest M²⁺ ions into the parent MPX3 compound could enhance properties for applications in catalysis or spintronics. Experimental and theoretical studies have shown that doping can significantly improve the catalytic properties of MPX3 for reactions like HER, [86] and doping with elements having filled d-shells can block the AFM interaction between neighboring M2+ ions, promoting a FM state.[119] b) High-entropy MPX3 alloys: A systematic and intensive theoretical analysis is needed to develop strategies for synthesizing highentropy MPX₃ alloys with tailored properties.^[112] These alloys could have diverse applications, from catalysis and sensing to

26884046, 0, Downloaded from https://onlinelibrary.wiley.com/doi/10.1002/smsc.202500307 by Ruder Boskovic Institute, Wiley Online Library on [09/10/2025]. See the Terms and Conditions (https://onlinelibrary.wiley.com/erms-and-conditions) on Wiley Online Library for rules of use; OA articles are governed by the applicable Creative Commons License

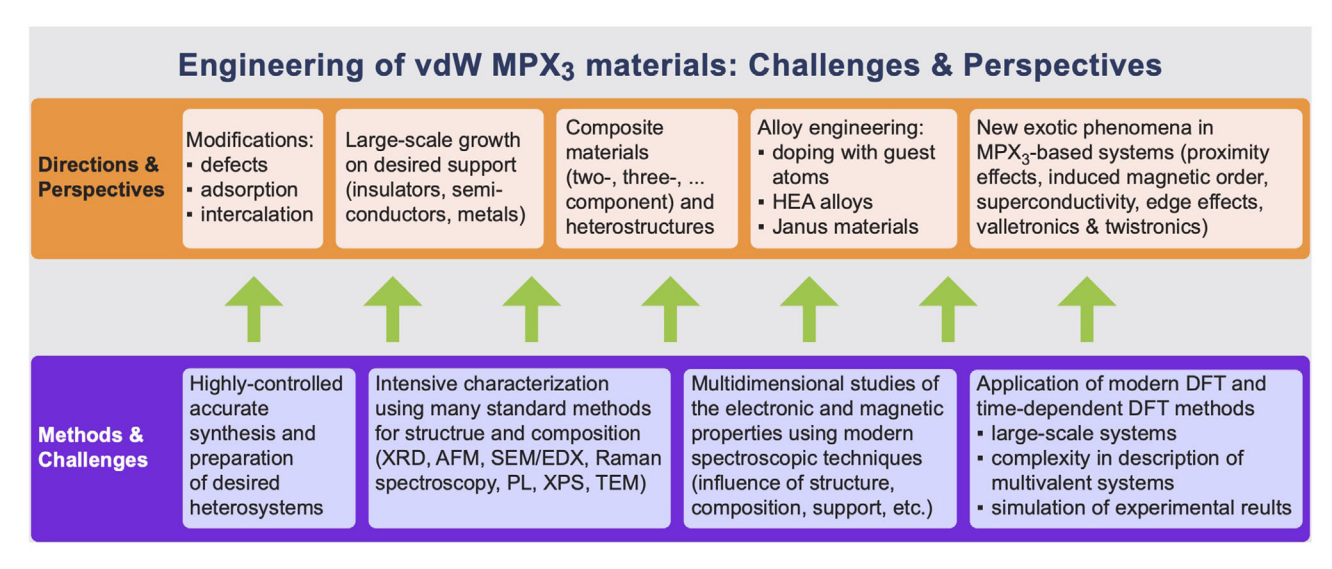


Figure 12. Challenges and perspectives in engineering of vdW MPX₃ materials.

spintronics. c) Janus MPX₃ materials: The hexagonal lattice of M²⁺ ions in MPX₃ is sandwiched between oppositely oriented PX₃ pyramids, leading to the concept of Janus MPX3 materials. These materials, where the top and bottom of the MPX3 layer are terminated with different chalcogens, have gained attention due to their unique properties, such as strong Rashba spin splitting, large piezoelectric effects, and enhanced catalytic performance. Although bulk MPX₃ Janus compounds may not be feasible, [125,126] a promising strategy involves growing ML-thick MPX3 on a desired support and replacing one layer of chalcogen atoms. This approach, successful in transition metal dichalcogenides, shows great potential for MPX₃ Janus material synthesis. [127,128] 3) Detailed and reliable studies of the electronic structure of MPX3 and their derivatives remain scarce in the literature, often due to the challenges associated with the quality of the synthesized samples and potential charging effects caused by the wide bandgap. Timeresolved spectroscopic studies are particularly valuable in this context, as they can provide new insights into the formation of metastable states in MPX3 materials. For example, such studies could help explore light-induced FM-to-AFM transitions.^[129–131] Additionally, time-resolved spectroscopic methods can be applied to investigate the mechanisms driving changes in the electronic, optical, and magnetic properties of MPX₃ during modifications, as discussed in this review. This knowledge will be crucial for tailoring these materials to specific applications. 4) All of the aforementioned directions concerning the synthesis and experimental investigation of MPX3-based systems must be accompanied by accurate and well-founded theoretical studies. However, theoretical analysis of the structural, electronic and magnetic modifications in MPX₃ through the discussed approaches remains a highly complex task.

First, any investigation of modified systems must be grounded in accurate modeling of the pristine compounds. This is particularly challenging in the case of MPX₃, which can be considered a multivalent system featuring three types of bonding—covalent, ionic, and vdW.^[20] MPX₃ materials also belong to the class of magnetic semiconductors, where accurate prediction of both

the bandgap and their rich magnetic behavior can be particularly demanding. Consequently, a significant number of theoretical studies and database entries on MPX₃ suffer from notable inaccuracies. These include incorrect predictions of the ground state (e.g., mistakenly identifying MPX₃ as metallic or FM), incorrect crystallographic data leading to misidentified Brillouin zones, and inconsistencies between the presented DOS and band structures. Additionally, the use of nonphysical computational parameters—such as arbitrarily chosen Hubbard *U* values in DFT calculations—often leads to misleading results aimed at reproducing desired effects rather than reflecting physical reality.

Second, for all considered modifications—defects, adsorption, and intercalation—it is essential to construct appropriately sized supercells with realistic periodicities. This enables accurate modeling of experimental conditions, such as reasonable concentrations of defects, adsorbates, or intercalated species, and proper lattice matching in heterostructures. It is critical that: 1) all individual components of a heterostructure are correctly described independently, $^{[132]}$ and 2) the chosen theoretical approaches consistently reproduce key experimental observables (e.g., lattice constants, bandgaps, magnetic moments) using a coherent set of computational parameters, including the exchange—correlation functional, U value, k-point mesh, and dispersion correction scheme.

Finally, the modeling of structural and spectroscopic properties in MPX₃-based systems deserves special attention, particularly in the context of reproducibility. Structural characterization can benefit greatly from simulations of scanning probe microscopy data, which provide both atomic-scale resolution and orbital-specific insights. Given the strong correlation effects present in MPX₃ compounds, the interpretation of spectroscopic data—such as XPS, NEXAFS, and time-resolved photoemission^[53]—offers valuable information on the electronic, optical, and magnetic properties of these materials and heterosystems. Particular focus should be placed on excitonic effects, [134,135] which are pronounced in MPX₃ and represent a powerful tool for probing and understanding various phenomena in vdW heterostructures.

26884046, 0, Downloaded from https://onlinelibrary.wiley.com/doi/10.1002/smsc.202500307 by Ruder Boskovic Institute, Wiley Online Library on [09/10/2025]. See the Terms

and Conditions (https://onlinelibrary.wiley.com/term

and-conditions) on Wiley Online Library for rules of use; OA articles are governed by the applicable Creative Commons I



Acknowledgements

Y.D. acknowledges the support by the project Centre for Advanced Laser Techniques (CALT), co-funded by the European Union through the European Regional Development Fund under the Competitiveness and Cohesion Operational Programme (grant no. KK.01.1.1.05.0001). E.V. acknowledges the support by the European Union's NextGenerationEU program.

Open access publishing facilitated by Institut Ruder Boskovic, as part of the Wiley - National and University Library in Zagreb Consortium Croatian Academic and Research Libraries Consortium agreement.

Conflict of Interest

The authors declare no conflict of interest.

Author Contributions

Yuriy Dedkov: conceptualization (equal); writing—original draft (equal); writing—review and editing (equal). Elena Voloshina: conceptualization (equal); writing—original draft (equal); writing—review and editing (equal).

Keywords

adsorption, defects, intercalation, trichalcogenides

Received: May 30, 2025 Revised: July 30, 2025 Published online:

- [1] S. Lin, G. Bai, Z. Liu, Z. Xu, Z. Hu, Adv. Condens. Matter Phys. 2018, 2018, 176029.
- [2] W. Ahmad, A. K. Tareen, K. Khan, M. Khan, Q. Khan, Z. Wang, M. Maqbool, Appl. Mater. Today 2023, 30, 101717.
- [3] P. Kumbhakar, J. S. Jayan, A. S. Madhavikutty, P. Sreeram, A. Saritha, T. Ito, C. S. Tiwary, iScience 2023, 26, 106671.
- [4] V. B. Mbayachi, E. Ndayiragije, T. Sammani, S. Taj, E. R. Mbuta, A. U. Khan, Results Chem. 2021, 3, 100163.
- [5] K. S. Novoselov, A. K. Geim, S. V. Morozov, D. Jiang, M. I. Katsnelson, I. V. Grigorieva, S. V. Dubonos, A. A. Firsov, Nature 2005, 438, 197.
- [6] Y. Zhang, Y.-W. Tan, H. L. Stormer, P. Kim, Nature 2005, 438, 201.
- [7] A. K. Geim, K. S. Novoselov, Nat. Mater. 2007, 6, 183.
- [8] J.-H. Chen, C. Jang, S. Xiao, M. Ishigami, M. S. Fuhrer, Nat. Nanotechnol. 2008, 3, 206.
- [9] K. S. Novoselov, Z. Jiang, Y. Zhang, S. V. Morozov, H. L. Stormer, U. Zeitler, J. C. Maan, G. S. Boebinger, P. Kim, A. K. Geim, Science 2007, 315, 1379.
- [10] Y. S. Dedkov, M. Fonin, C. Laubschat, Appl. Phys. Lett. 2008, 92, 052506.
- [11] E. Sutter, P. Albrecht, F. E. Camino, P. Sutter, Carbon 2010, 48, 4414.
- [12] N. Tombros, C. Jozsa, M. Popinciuc, H. T. Jonkman, B. J. V. Wees, *Nature* **2007**, 448, 571.
- [13] M. Drogeler, F. Volmer, M. Wolter, B. Terres, K. Watanabe, T. Taniguchi, G. Güntherodt, C. Stampfer, B. Beschoten, *Nano Lett.* 2014, 14, 6050.
- [14] A. Bostwick, T. Ohta, J. L. McChesney, K. V. Emtsev, T. Seyller, K. Horn, E. Rotenberg, New J. Phys. 2007, 9, 385.
- [15] E. Y. Andrei, A. H. MacDonald, Nat. Mater. 2020, 19, 1265.

- [16] J. M. Park, Y. Cao, K. Watanabe, T. Taniguchi, P. Jarillo-Herrero, Nature 2021, 590, 249.
- [17] M. A. Kharadi, G. F. A. Malik, F. A. Khanday, K. A. Shah, S. Mittal, B. K. Kaushik, ECS J. Solid State Sc. 2020, 9, 115031.
- [18] A. Carvalho, M. Wang, X. Zhu, A. S. Rodin, H. Su, A. H. Castro Neto, Nat. Rev. Mater. 2016, 1, 16061.
- [19] S. Manzeli, D. Ovchinnikov, D. Pasquier, O. V. Yazyev, A. Kis, Nat. Rev. Mater. 2017, 2, 17033.
- [20] Y. Dedkov, Y. Guo, E. Voloshina, Electron. Struct. 2023, 5, 043001.
- [21] M. A. Susner, M. Chyasnavichyus, M. A. McGuire, P. Ganesh, P. Maksymovych, Adv. Mater. 2017, 29, 1602852.
- [22] F. Wang, T. A. Shifa, P. Yu, P. He, Y. Liu, F. Wang, Z. Wang, X. Zhan, X. Lou, F. Xia, J. He, Adv. Funct. Mater. 2018, 28, 1802151.
- [23] H. Wang, P. Cheng, B. Wu, Y. Yan, P. Schaaf, Z. Sofer, D. Wang, Adv. Funct. Mater. 2024, 34, 2407432.
- [24] W. F. Io, S. Y. Pang, L. W. Wong, Y. Zhao, R. Ding, J. Mao, Y. Zhao, F. Guo, S. Yuan, J. Zhao, J. Yi, J. Hao, Nat. Commun. 2023, 14, 7304.
- [25] X. Wang, Z. Shang, C. Zhang, J. Kang, T. Liu, X. Wang, S. Chen, H. Liu, W. Tang, Y.-J. Zeng, J. Guo, Z. Cheng, L. Liu, D. Pan, S. Tong, B. Wu, Y. Xie, G. Wang, J. Deng, T. Zhai, H.-X. Deng, J. Hong, J. Zhao, *Nat. Commun.* 2023, 14, 840.
- [26] H.-Y. Zhong, Y. Chai, X. Lu, P.-W. Huang, B.-C. Chen, K.-Z. Du, X.-H. Wu, Chem. Eng. J. 2023, 475, 145990.
- [27] H. Zhang, G. Meng, Q. Liu, Y. Luo, M. Niederberger, L. Feng, J. Luo, X. Liu, Small 2023, 19, e2303165.
- [28] Y. Zhao, C. Bao, Y. Zhang, K. Du, W. Huang, C. Su, Mater. Lett. 2022, 324, 132687.
- [29] K. Pramoda, C. N. R. Rao, J. Mater. Chem. A 2023, 11, 16933.
- [30] N. Ismail, M. Madian, A. El-Meligi, J. Alloy. Compd. 2014, 588, 573.
- [31] I. Cabria, A. El-Meligi, Int. J. Hydrogen Energy 2018, 43, 5903.
- [32] K.-Z. Du, X.-Z. Wang, Y. Liu, P. Hu, M. I. B. Utama, C. K. Gan, Q. Xiong, C. Kloc, ACS Nano 2016, 10, 1738.
- [33] S. Huang, Z. Qiu, J. Zhong, S. Wu, X. Han, W. Hu, Z. Han, W. N. Cheng, Y. Luo, Y. Meng, Z. Hu, X. Zhou, S. Guo, J. Zhu, X. Zhao, C. C. Li, Adv. Mater. 2024, 36, e2405170.
- [34] R. Wang, J. Huang, X. Zhang, J. Han, Z. Zhang, T. Gao, L. Xu, S. Liu, P. Xu, B. Song, ACS Nano 2022, 16, 3593.
- [35] Z. Muhammad, J. Szpakowski, G. Abbas, L. Zu, R. Islam, Y. Wang, F. Wali, A. Karmakar, M. R. Molas, Y. Zhang, L. Zhu, W. Zhao, H. Zhang, 2D Mater. 2023, 10, 025001.
- [36] C. Tang, D. He, N. Zhang, X. Song, S. Jia, Z. Ke, J. Liu, J. Wang, C. Jiang, Z. Wang, X. Huang, X. Xiao, Energy Environ. Mater. 2022, 5, 899.
- [37] J. Yang, Y. Zhou, Q. Guo, Y. Dedkov, E. Voloshina, RSC Adv. 2020, 10, 851.
- [38] S. Lee, J. Park, Y. Choi, K. Raju, W.-T. Chen, R. Sankar, K.-Y. Choi, Phys. Rev. B 2021, 104, 174412.
- [39] H. Han, H. Lin, W. Gan, Y. Liu, R. Xiao, L. Zhang, Y. Li, C. Zhang, H. Li, Appl. Phys. Lett. 2023, 122, 033101.
- [40] Y. Lai, Z. Song, Y. Wan, M. Xue, C. Wang, Y. Ye, L. Dai, Z. Zhang, W. Yang, H. Du, J. Yang, *Nanoscale* 2019, 11, 5163.
- [41] Y. Guo, J. Yang, J. Zhou, N. Zhu, Y. Jin, G. Thiele, A. Preobrajenski, E. Voloshina, Y. Dedkov, J. Phys. Chem. C 2024, 128, 7830.
- [42] J. B. Goodenough, Phys. Rev. 1955, 100, 564.
- [43] J. Kanamori, J. Appl. Phys. 1960, 31, S14.
- [44] P. W. Anderson, Phys. Rev. 1959, 115, 2.
- [45] J. Zaanen, G. A. Sawatzky, J. W. Allen, Phys. Rev. Lett. 1985, 55, 418.
- [46] A. Kamata, K. Noguchi, K. Suzuki, H. Tezuka, T. Kashiwakura, Y. Ohno, S.-I. Nakai, J. Phys. Soc. Jpn. 1997, 66, 401.
- [47] J. Strasdas, B. Pestka, M. Rybak, A. K. Budniak, N. Leuth, H. Boban, V. Feyer, I. Cojocariu, D. Baranowski, J. Avila, P. Dudin, A. Bostwick, C. Jozwiak, E. Rotenberg, C. Autieri, Y. Amouyal, L. Plucinski, E. Lifshitz, M. Birowska, M. Morgenstern, *Nano Lett.* 2023, 23, 10342.

26884046, 0, Downloaded from https://onlinelibrary.wiley.com/doi/10.1002/smsc.202500307 by Ruder Boskovic Institute, Wiley Online Library on [09/10/2025]. See the Terms and Conditions (https://onlinelibrary.wiley.com/terms

and-conditions) on Wiley Online Library for rules of use; OA articles are governed by the applicable Creative Commons I

www advancedsciencenews com

www.small-science-journal.com

- [48] Y. Li, Y. Li, Q. Zhang, N. Su, J. Sun, N. Xiao, Y. Liu, Y. Liu, H. Liu, L. Zhao, Appl. Mater. Today 2024, 37, 102129.
- [49] Y. Jin, M. Yan, T. Kremer, E. Voloshina, Y. Dedkov, Sci. Rep. 2022, 12, 735.
- [50] M. Yan, Y. Jin, E. Voloshina, Y. Dedkov, J. Phys. Chem. Lett. 2023, 14, 9774.
- [51] A. Koitzsch, T. Klaproth, S. Selter, Y. Shemerliuk, S. Aswartham, O. Janson, B. Büchner, M. Knupfer, npj Quantum Mater. 2023, 8, 27.
- [52] B. Pestka, J. Strasdas, G. Bihlmayer, A. K. Budniak, M. Liebmann, N. Leuth, H. Boban, V. Feyer, I. Cojocariu, D. Baranowski, S. Mearini, Y. Amouyal, L. Waldecker, B. Beschoten, C. Stampfer, L. Plucinski, E. Lifshitz, P. Kratzer, M. Morgenstern, ACS Nano 2024, 18, 32924
- [53] J. E. Nitschke, L. Sternemann, M. Gutnikov, K. Schiller, E. Coronado, A. Omar, G. Zamborlini, C. Saraceno, M. Stupar, A. M. Ruiz, D. L. Esteras, J. J. Baldov, F. Anders, M. Cinchetti, *Newton* 2025, 1, 100019.
- [54] T. Klaproth, S. Aswartham, Y. Shemerliuk, S. Selter, O. Janson, J. V. D. Brink, B. Büchner, M. Knupfer, S. Pazek, D. Mikhailova, A. Efimenko, R. Hayn, A. Savoyant, V. Gubanov, A. Koitzsch, *Phys. Rev. Lett.* 2023, 131, 256504.
- [55] Y. Jin, Y. Jin, K. Li, M. Yan, Y. Guo, Y. Zhou, A. Preobrajenski, Y. Dedkov, E. Voloshina, J. Phys. Chem. Lett. 2022, 13, 10486.
- [56] E. Voloshina, Y. Jin, Y. Dedkov, Chem. Phys. Lett. 2023, 823, 140511.
- [57] R. Brec, Solid State Ion. 1986, 22, 3.
- [58] F. Wang, T. A. Shifa, P. He, Z. Cheng, J. Chu, Y. Liu, Z. Wang, F. Wang, Y. Wen, L. Liang, J. He, Nano Energy 2017, 40, 673.
- [59] J. Zhou, C. Zhu, Y. Zhou, J. Dong, P. Li, Z. Zhang, Z. Wang, Y.-C. Lin, J. Shi, R. Zhang, Y. Zheng, H. Yu, B. Tang, F. Liu, L. Wang, L. Liu, G.-B. Liu, W. Hu, Y. Gao, H. Yang, W. Gao, L. Lu, Y. Wang, K. Suenaga, G. Liu, F. Ding, Y. Yao, Z. Liu, Nat. Mater. 2023, 22, 450.
- [60] Z. Wu, S. Xu, Y. Zhou, Q. Guo, Y. Dedkov, E. Voloshina, Adv. Theory Simul. 2021, 4, 2100182.
- [61] S. Xu, Z. Wu, Y. Dedkov, E. Voloshina, J. Phys. Condens. Matter 2021, 33, 354001.
- [62] J. Koster, A. Storm, M. Ghorbani-Asl, S. Kretschmer, T. E. Gorelik, A. V. Krasheninnikov, U. Kaiser, J. Phys. Chem. C 2022, 126, 15446.
- [63] A. Storm, J. Koster, M. Ghorbani-Asl, S. Kretschmer, T. E. Gorelik, M. K. Kinyanjui, A. V. Krasheninnikov, U. Kaiser, ACS Nano 2023, 17, 4250.
- [64] A. Storm, J. Koster, M. Ghorbani-Asl, S. Kretschmer, T. E. Gorelik, A. V. Krasheninnikov, U. Kaiser, J. Phys. Chem. C 2023, 127, 24713.
- [65] W. Bai, Z. Hu, C. Xiao, J. Guo, Z. Li, Y. Zou, X. Liu, J. Zhao, W. Tong, W. Yan, Z. Qu, B. Ye, Y. Xie, J. Am. Chem. Soc. 2020, 142, 10849.
- [66] F. Wang, N. Mathur, A. N. Janes, H. Sheng, P. He, X. Zheng, P. Yu, A. J. DeRuiter, J. R. Schmidt, J. He, S. Jin, Sci. Adv. 2021, 7, eabj4086.
- [67] S. Sharma, H. M. Zeeshan, M. Panahi, Y. Jin, M. Yan, Y. Jin, K. Li, P. Zeller, A. Efimenko, A. Makarova, D. Smirnov, B. Paulus, E. Voloshina, Y. Dedkov, 2D Mater. 2023, 10, 014008.
- [68] B. Song, K. Li, Y. Yin, T. Wu, L. Dang, M. Cabán-Acevedo, J. Han, T. Gao, X. Wang, Z. Zhang, J. R. Schmidt, P. Xu, S. Jin, ACS Catal. 2017, 7, 8549.
- [69] Y. Guo, G. Cai, J. Zhou, J. Yang, E. Voloshina, Y. Dedkov, ChemPhysChem 2024, 25, e202400039.
- [70] L. Ji, L. Chang, Y. Zhang, S. Mou, T. Wang, Y. Luo, Z. Wang, X. Sun, ACS Catal. 2019, 9, 9721.
- [71] X. Zhang, X. Zhao, D. Wu, Y. Jing, Z. Zhou, Adv. Sci. 2016, 3, 1600062.
- [72] C.-F. Du, Q. Liang, R. Dangol, J. Zhao, H. Ren, S. Madhavi, Q. Yan, Nano-Micro. Lett. 2018, 10, 67.
- [73] R. Gusmão, Z. Sofer, M. Pumera, Angew. Chem., Int. Ed. 2019, 58, 9326.
- [74] K. Alam, T. Das, S. Chakraborty, P. Sen, Phys. Chem. Chem. Phys. 2021, 23, 23967.
- [75] T. Das, K. Alam, S. Chakraborty, P. Sen, Int. J. Hydrogen. Energ. 2021, 46, 37928.

- [76] J. Dai, K. Wang, E. Voloshina, Y. Dedkov, B. Paulus, ACS Omega 2023, 8, 33920.
- [77] I. Brotons-Alcázar, R. Torres-Cavanillas, M. Morant-Giner, M. Cvikl, S. Mañas-Valero, A. Forment-Aliaga, E. Coronado, *Dalton Trans*. 2021, 50, 16281.
- [78] R. Kumar, R. N. Jenjeti, S. Sampath, ACS Sens. 2020, 5, 404.
- [79] R. Kumar, R. N. Jenjeti, V. S. K. Choutipalli, V. Subramanian, S. Sampath, Sens. Actuators, B 2021, 347, 130633.
- [80] M. Jiang, K. Xu, N. Liao, H. Zhou, Appl. Surf. Sci. 2021, 543, 148846.
- [81] K. Wang, K. Ren, Y. Cheng, S. Chen, G. Zhang, Mater. Horiz. 2022, 9, 2384.
- [82] X. Li, X. Wu, J. Yang, J. Am. Chem. Soc. 2014, 136, 11065.
- [83] Y. Jin, M. Yan, Y. Dedkov, E. Voloshina, J. Mater. Chem. C 2022, 10, 3812.
- [84] N. Wang, J. Chen, Y. An, Q. Zhan, S.-J. Gong, npj Spintron. 2024, 2, 60.
- [85] A. Dhanarajgopal, P.-C. Chang, S.-Y. Liu, T.-H. Chuang, D.-H. Wei, C.-C. Kuo, C.-N. Kuo, C. S. Lue, W.-C. Lin, Appl. Surf. Sci. 2021, 567, 150864
- [86] S. Wang, B. Xiao, S. Shen, K. Song, Z. Lin, Z. Wang, Y. Chen, W. Zhong, *Nanoscale* 2020, 12, 14459.
- [87] K. Li, M. Yan, Y. Jin, Y. Jin, Y. Guo, E. Voloshina, Y. Dedkov, J. Phys. Chem. Lett. 2023, 14, 57.
- [88] R. Schollhorn, Physica B+C 1980, 99, 89.
- [89] V. Grasso, L. Silipigni, Riv. del Nuovo Cimento 2002, 25, 1.
- [90] R. Brec, D. M. Schleich, G. Ouvrard, A. Louisy, J. Rouxel, *Inorg. Chem.* 1979, 10, 1814.
- [91] R. Clement, M. L. H. Green, J. Chem. Soc., Dalton Trans. 1979, 1979, 1566.
- [92] R. Clement, L. Lomas, J. P. Audiere, Chem. Mater. 1990, 2, 641.
- [93] S. Otani, M. Shimada, F. Kanamaru, M. Koizumi, *Inorg. Chem.* 1980, 19, 1249.
- [94] M. Barj, C. Sourisseau, G. Ouvrard, R. Brec, Solid State Ion. 1983, 11, 179.
- [95] M. Bernasconi, G. L. Marra, G. Benedek, L. Miglio, M. Jouanne, C. Julien, M. Scagliotti, M. Balkanski, Phys. Rev. B 1988, 38, 12089.
- [96] G. M. Curro, V. Grasso, F. Neri, L. Silipigni, Il Nuovo Cimento D 1995, 17, 37.
- [97] M. H. Whangbo, R. Brec, G. Ouvrard, J. Rouxel, *Inorg. Chem.* 1985, 24, 2459.
- [98] M. B. Dines, Mater. Res. Bull. 1975, 10, 287.
- [99] C. Berthier, Y. Chabre, M. Minier, Solid State Commun. 1978, 28, 327.
- [100] G. A. Fatseas, M. Evain, G. Ouvrard, R. Brec, M. H. Whangbo, *Phys. Rev. B* 1987, 35, 3082.
- [101] I. Kerrache, C. Julien, C. Sourisseau, Solid State Ion. 1996, 92, 37.
- [102] G. Ouvrard, Mater. Sci. Eng.: B 1989, 3, 81.
- [103] G. Ouvrard, E. Prouzet, R. Brec, S. Benazeth, H. Dexpert, J. Solid State Chem. 1990, 86, 238.
- [104] S. Y. Kim, T. Y. Kim, L. J. Sandilands, S. Sinn, M.-C. Lee, J. Son, S. Lee, K.-Y. Choi, W. Kim, B.-G. Park, C. Jeon, H.-D. Kim, C.-H. Park, J.-G. Park, S. J. Moon, T. W. Noh, Phys. Rev. Lett. 2018, 120, 136402.
- [105] M. Yan, Y. Jin, Z. Wu, A. Tsaturyan, A. Makarova, D. Smirnov, E. Voloshina, Y. Dedkov, J. Phys. Chem. Lett. 2021, 12, 2400.
- [106] S. Pazek, A. Efimenko, R. Felix, M. Roslova, C. J. Querebillo, M. V. Gorbunov, A. Ovchinnikov, A. Koitzsch, C. Escudero, Y. Shemerliuk, S. Aswartham, B. Buchner, A. Omar, D. Mikhailova, J. Mater. Chem. A 2024, 12, 3523.
- [107] D. Yang, R. F. Frindt, J. Mater. Res. 2000, 15, 2408.
- [108] L. Silipigni, V. Grasso, G. D. Luca, L. M. Scolaro, G. Salvato, J. Appl. Phys. 2005, 98, 043307.
- [109] L. Silipigni, T. Quattrone, L. Schiro, V. Grasso, L. M. Scolaro,
 G. D. Luca, G. Salvato, J. Appl. Phys. 2008, 104, 123711.
- [110] L. Silipigni, G. D. Marco, G. Salvato, V. Grasso, Appl. Surf. Sci. 2005, 252, 1998.

Soc. 2021, 143, 7042.



www.small-science-iournal.com

- [128] J. Picker, M. Ghorbani-Asl, M. Schaal, S. Kretschmer, F. Otto, M. Gruenewald, C. Neumann, T. Fritz, A. V. Krasheninnikov,
- [111] T. Ying, T. Yu, Y.-S. Shiah, C. Li, J. Li, Y. Qi, H. Hosono, J. Am. Chem. [112] T. Ying, T. Yu, Y. Qi, X. Chen, H. Hosono, Adv. Sci. 2022, 9, 2203219.
- [113] X. Chen, J. Wang, T. Ying, D. Huang, H. Gou, Q. Zhang, Y. Li, H. Hosono, J.-G. Guo, X. Chen, Phys. Rev. B 2022, 106, 184502.
- [114] P. E. Meza, A. Iyer, R. D. Reis, Y. Liu, M. Kanatzidis, V. P. Dravid, Microsc. Microanal. 2024, 30, ozae044.660.
- [115] X. Zhang, H. Zhou, X. Su, X. Chen, C. Yang, J. Qin, M. Inokuchi, J. Alloys Compd. 2007, 432, 247.
- [116] P. A. Joy. S. Vasudevan, Phys. Rev. B 1992, 46, 5425.
- [117] N. Sivadas, M. W. Daniels, R. H. Swendsen, S. Okamoto, D. Xiao, Phys. Rev. B 2015, 91, 235425.
- [118] Y. Sugita, T. Miyake, Y. Motome, Phys. Rev. B 2018, 97, 035125.
- [119] J. Yang, Y. Zhou, Y. Dedkov, E. Voloshina, Adv. Theory Simul. 2020, 3, 2000228
- [120] R. Basnet, D. Ford, K. TenBarge, J. Lochala, J. Hu, J. Phys. Condens. Matter. 2022, 34, 434002.
- [121] D. Tezze, J. M. Pereira, Y. Asensio, M. Ipatov, F. Calavalle, F. Casanova, A. M. Bittner, M. Ormaza, B. Martn-Garca, L. E. Hueso, M. Gobbi, Nanoscale 2022, 14, 1165.
- [122] M. Mi, X. Zheng, S. Wang, Y. Zhou, L. Yu, H. Xiao, H. Song, B. Shen, F. Li, L. Bai, Y. Chen, S. Wang, X. Liu, Y. Wang, Adv. Funct. Mater. **2022**, 32, 2112750.
- [123] Y. Ou, X. Li, J. Kopaczek, A. Davis, G. Jackson, M. Sayyad, F. Liu, S. A. Tongay, Adv. Phys. Res. 2024, 4, 2570003.
- [124] D. Tezze, J. M. Pereira, D. Tutar, M. Ramos, J. Regner, P. Gargiani, F. Schiller, F. Casanova, A. Alegria, B. Martn-Garca, H. Sahin, Z. Sofer, M. Ormaza, L. E. Hueso, M. Gobbi, Adv. Funct. Mater. 2024, 35, 2412771.
- [125] D. W. Boukhvalov, Phys. Chem. Chem. Phys. 2022, 24, 9836.
- [126] Y. Jin, M. Yan, Y. Jin, K. Li, Y. Dedkov, E. Voloshina, J. Phys. Chem. C **2022**, *126*, 16061.
- [127] Z. Gan, I. Paradisanos, A. Estrada-Real, J. Picker, E. Najafidehaghani, F. Davies, C. Neumann, C. Robert, P. Wiecha, K. Watanabe, T. Taniguchi, X. Marie, J. Biskupek, M. Mundszinger, R. Leiter, U. Kaiser, A. V. Krasheninnikov, B. Urbaszek, A. George, A. Turchanin, Adv. Mater. 2022, 34, e2205226.

- A. Turchanin, Nano Lett. 2025, 25, 3330.
- [129] E. Ergecen, B. Ilyas, J. Kim, J. Park, M. B. Yilmaz, T. Luo, D. Xiao, S. Okamoto, J.-G. Park, N. Gedik, Proc. Natl. Acad. Sci. 2023, 120, e2208968120.
- [130] F. Mertens, D. Mönkebüscher, U. Parlak, C. Boix-Constant, S. Mañas-Valero, M. Matzer, R. Adhikari, A. Bonanni, E. Coronado, A. M. Kalashnikova, D. Bossini, M. Cinchetti, Adv. Mater. 2023, 35, 2208355.
- [131] A. Zong, Q. Zhang, F. Zhou, Y. Su, K. Hwangbo, X. Shen, Q. Jiang, H. Liu, T. E. Gage, D. A. Walko, M. E. Kozina, D. Luo, A. H. Reid, J. Yang, S. Park, S. H. Lapidus, J.-H. Chu, I. Arslan, X. Wang, D. Xiao, X. Xu, N. Gedik, H. Wen, Nature 2023, 620, 988.
- [132] Y. Dedkov, E. Voloshina, Appl. Phys. Rev. 2024, 11, 041409.
- [133] M. Fonin, V. Enenkel, I. S. Rakic, Y. Dedkov, E. Voloshina, J. Phys. Chem. C 2025, 129, 5762.
- [134] S. Kang, K. Kim, B. H. Kim, J. Kim, K. I. Sim, J.-U. Lee, S. Lee, K. Park, S. Yun, T. Kim, A. Nag, A. Walters, M. Garcia-Fernandez, J. Li, L. Chapon, K.-J. Zhou, Y.-W. Son, J. H. Kim, H. Cheong, J.-G. Park, Nature 2020, 583, 785.
- [135] M. Birowska, P. E. F. Junior, J. Fabian, J. Kunstmann, Phys. Rev. B 2021, 103, L121108.
- [136] R. Xu, G. Fu, W. Ding, Y. Li, G. Yang, P. Yu, S. Li, P. Liu, Adv. Sci. **2025**, *12*, 2501836.
- [137] D. Chen, C. Wang, C. Peng, Phys. Chem. Chem. Phys. 2024, 26, 8436.
- [138] D. Upreti, R. Basnet, M. M. Sharma, S. K. Chhetri, G. Acharya, M. R. U. Nabi, J. Sakon, B. Da, M. Mortazavi, J. Hu, J. Phys. Condens. Matter 2025, 37, 135805.
- [139] X. Feng, Z. Guo, X. Yan, J. Deng, D. Wu, Z. Zhang, F. Sun, W. Yuan, Mater. Chem. Front. 2021, 5, 2715.
- [140] C. Li, Z. Hu, X. Hou, S. Xu, Z. Wu, K. Du, S. Li, X. Xu, Y. Chen, Z. Wang, T. Mu, T.-L. Xia, Y. Guo, B. Normand, W. Yu, Y. Cui, Phys. Rev. B 2024, 109, 184407.
- [141] L. Jun, D. Yao-Dong, H. Yun, H. Hong-Bo, X. Fan, X. Yuan-Fu, Chin. Phys. Lett. 2004, 21, 386.



Yuriy Dedkov is a tenured Scientific Advisor (equiv. to Full Professor with tenure) at the Institute of Physics in Zagreb (Croatia) since September 2024. He obtained his Ph.D. degree in 2004 from RWTH Aachen (Germany) and earned his Habilitation degree in 2013 form TU Dresden (Germany). He has a broad experience in many surface-science techniques with specialisation in spin- and angle-resolved photoelectron spectroscopy and scanning probe microscopy. Since 2008 his research is focused on different two-dimensional (2D) materials and heterostrcutures. He started several directions in this field, including spin-related effects in the graphene-metal systems as well as demonstration for the first time the inert properties of graphene. In 2017-2024 he led research group in Shanghai University (P. R. China) where he started studies of new quasi-2D material which are the subject of the present review. For his pioneering works, he was awarded to the Gaede Prize of the German Vacuum Society (2014) and Shanghai 1000 Talent award (2017).



Elena Voloshina is Scientific Advisor (equiv. to Full Professor) at Ruđer Bošković Institute (Zagreb, Croatia) since November 2024. She completed her Ph.D. study at Rostov State University (Russia) in 2001 and earned her Habilitation degree from FU Berlin (Germany) in 2023. When working at top research institutes and universities in Germany and China (2002-2024), she gained extensive experience in developing and applying various theoretical methods to study the electronic structure of a wide range of systems. At present, her research is focused on the study of the crystallographic structure and electronic properties of different low-dimensional objects, and particularly two-dimensional (2D) materials and systems on their basis. For her contributions in this field she was distinguished by the Shanghai 1000 Talent award (2018).